THE MECHANISMS OF SEA ICE MELT POND FORMATION AND EVOLUTION

by

Chris Polashenski[1,*], Donald Perovich[2], and Zoe Courville[2]

[1]Dartmouth College Thayer School of Engineering, HB 8000 Hanover, NH 03755

[2] Terrestrial and Cryospheric Sciences Branch, USACRREL, 72 Lyme Rd, Hanover, NH 03755

*Contact Information of Corresponding Author: chris.polashenski@gmail.com

Abstract

A series of observations were made on melting first year sea ice near Barrow, AK to explore the seasonal evolution of melt pond coverage. Observations of pond coverage, albedo, and ice properties are combined with terrestrial LiDAR measurements of surface topography and meltwater balance to quantitatively identify the timing and role of mechanisms driving pond coverage. The formation of interposed fresh ice is found to eliminate meltwater percolation through early pond formation and allow widespread ponding well above sea level. Pond drainage to sea level occurs principally by horizontal meltwater transport over the ice surface to macroscopic flaws. Freeboard loss, caused by buoyancy decline as the ice thins, controls pond growth late in the melt season after percolation begins. The majority of the macroscopic flaws that drain melt ponds to sea level are observed to develop from brine drainage channels within the ice. A simple thermodynamic model of meltwater percolation illustrates that fresh meltwater inflow causes pores in the ice to either shrink and freeze shut or enlarge based on initial size and ice temperature. This threshold behavior of pore diameter controls both the formation of interposed ice in smaller pores that block percolation and the enlargement of brine drainage channels that allow meltwater drainage. The results identify links between the temporal evolution of pond coverage and ice temperature, salinity, and thickness, providing new opportunities to realistically parameterize ponds and summer ice albedo within sea ice models.

1. Introduction

Shortly after the onset of sea ice melt in the Arctic, meltwater begins to collect on the ice surface in visible pools referred to as melt ponds. The pooling water alters the light scattering properties of the ice surface and dramatically lowers albedo wherever melt ponds form [Perovich et al., 2002a; Grenfell and Perovich 2004]. The lowered albedo, in turn, changes both the amount and the partitioning of solar energy in the ice-ocean system. Increased absorption of sunlight in the ice and the upper ocean accelerates ice melt [Perovich et al., 2003], while greater sunlight availability beneath the ice may enhance primary productivity [Light et al., 2008]. Ponded ice which is subsequently drained of meltwater rapidly reforms a surface scattering layer of loose, decaying ice crystals, and returns to a high albedo, similar to that of ice that never ponded [Perovich et al., 2002a]. The spatial coverage of melt ponds is therefore a predominate control of albedo and solar energy partitioning on melting Arctic sea ice [Eicken et al., 2004], and, because of the importance of albedo feedbacks in the Arctic, is a variable of considerable interest in climate modeling.

Despite the importance and ubiquitous presence of ponds during melt, relatively few comprehensive observations of pond coverage have been collected in the Arctic. Efforts to collect such data are limited by the hazards of operation on melting ice, difficulty differentiating ponds from open water in remote sensing [Fetterer and Untersteiner, 1998], and the persistent presence of low clouds during Arctic summer, which restrict aerial and satellite based observations [Perovich et al., 2002b]. The lack of a long term, intercomparable data set severely hampers any assessment of trends or potential feedbacks in the behavior of ponds, though it is generally conjectured that pond

coverage in the Arctic is increasing due to increased presence of first year ice (FYI) [Eicken et al., 2004]. Available observations show that spatial coverage of melt ponds is highly variable and dynamic, particularly early in the melt season and especially on FYI. Areal pond coverage on undeformed FYI has been observed to range from 0% to 75% at a single site, with rates of change as high as 35% coverage per day [Scharien and Yackel, 2005]. A compilation of multiple study results tracking pond coverage, presented in Figure 1, illustrates that both absolute pond coverage and seasonal evolution of pond coverage exhibit large inter-annual and spatial variability.

This variability presents significant challenges for realistic ice albedo simulation within sea ice and climate models. Semi-empirical ice albedo models, which set albedo based on seasonal transition points, rely on an assumption that the albedo between the transitions can be uniformly represented across ice types and locations. Such models represent changing seasonality well and can produce realistic annual energy fluxes when the selected summer ice albedo matches observations [Perovich et al., 2002a]. Substantial spatial variability in observed ponding behavior, however, suggests that fixed empirical representations of summer ice albedo likely lack generality for other ice types and locations. Temporal variability of melt pond coverage also creates substantial intra-annual discrepancies between modeled and observed albedo [Perovich et al., 2002a]. Linkages between pond coverage, albedo, and melt rates, which have the potential to result in significant pond-related albedo feedbacks, make even these short term deviations important. Ensuring realistic prediction of albedo will require incorporating the mechanisms that drive pond coverage into models. A substantial effort is already being undertaken to do this by improving both small and medium scale models of melt pond

93 coverage [Skyllingstad et al., 2009; Flocco and Feltham, 2007; Luthje et al., 2006; Taylor
94 and Feltham, 2004] and incorporating explicit melt pond parameterizations into albedo
95 calculations of global climate models [Flocco et al., 2010; Hunke and Lipscomb, 2010;
96 Pederson et al, 2009]. In the absence of basin wide pond observations and long term data
97 sets, supporting these efforts to create computationally efficient, yet physically
98 representative models, requires further advances in our understanding of the mechanisms
99 which drive the seasonal evolution of pond coverage.
100
101 **2. Background**
102 **2.1. The Stages of Pond Evolution**
103 Many factors are known to influence the development of melt ponds. When
104 thought of as a hydraulic feature, a melt pond can be represented as a volume of water
105 determined by the balance of inflows and outflows, distributed in the lowest points of
106 local topography. This meltwater accounting conceptualization, schematically shown in
107 Figure 2, reflects the general approach of some GCM pond parameterizations [Hunke and
108 Lipscomb, 2010; Pederson et al, 2009]. Inflow rates to ponds are determined by melt rate,
109 precipitation, and the size of a pond's catchement basin. Outflow rates depend on both
110 hydraulic head and the presence of outflow pathways. Outflow can proceed either by
111 vertical percolation through porosity in the ice or by horizontal movement of water across
112 the surface of the ice to macroscopic flaws, such as cracks, leads, seal breathing holes,
113 and as we describe later, enlarged brine channels. Topographic relief depends on myriad
114 factors, including deformation history, snow drifts, ice freeboard, and past seasons' melt,

115 but is generally known to be lower on un-deformed FYI than on un-deformed multiyear
116 ice (MYI).

117 Past observations have demonstrated that the evolution of seasonal pond coverage
118 is characterized by four general stages, defined by descriptions of pond behavior and
119 control mechanisms [Eicken et al., 2002]. The first stage begins with the onset of pond
120 formation and is characterized by a rapid rise in pond coverage as meltwater accumulates
121 on the surface of relatively impermeable ice. Pond volume is controlled by melt rate and
122 the loss of meltwater through lateral transport to cracks and flaws. Outflow pathways are
123 limited and ponds typically form well above sea level. Topographic relief of the ice,
124 which governs how meltwater is distributed on the ice surface, is predominantly dictated
125 by forces that occurred prior to the onset of melt such as deformation, snow drifting, and,
126 on MYI, hummock creation during previous melt seasons. Due to the topographic relief
127 created by hummocks, ponds on MYI tend to be confined to deeper pools with less
128 spatial coverage than on FYI where limited relief results in shallow, but widespread,
129 ponding. Pond coverage on undeformed FYI frequently spikes to 50% or more during
130 this period, while coverage on multiyear ice exhibits a more subdued peak. Because this
131 first stage results in very low albedo and coincides with near peak solar input in much of
132 the Arctic, its duration can be quite important to seasonal energy balance.

133 During the second stage, the majority of the ponds drop to sea level due to
134 increased outflow. Pond coverage drops substantially on FYI, but only slightly on
135 multiyear ice. Both percolation through the ice [Eicken et al., 2002] and continued
136 horizontal transport to macroscopic flaws [Scharien and Yackel, 2005] are cited as

137 significant causes of water loss during this time, though our data show that horizontal
138 transport dominated at our site.

139 During the third stage, ponds remain at sea level because outflow pathways are no
140 longer limiting, yet pond coverage on both ice types increases steadily, often to its
141 seasonal maximum. Many ponds melt through to the ocean, and the ice may decay
142 entirely. Meltwater balance becomes unimportant as a control mechanism because
143 outflow pathways are unlimited. Changes in topographic relief now play a larger role in
144 determining pond coverage. Increases in pond area during this time occur by creating
145 new areas where the local surface height is below freeboard. These areas may be created
146 either by lateral melt at the walls of the ponds or by a change in overall ice freeboard as
147 the ice thins and buoyancy force is lost.

148 The fourth stage, refreezing, is not restricted to the end of the season. At any time
149 during this seasonal evolution, changing atmospheric forcing may result in freezing
150 conditions, which can stop meltwater inflow and cause a skim of ice to form over many
151 ponds. A thick dusting of snow on top of this ice can temporarily erase the albedo effects
152 of the ponds [Grenfell and Perovich, 2004].

153

154 **2.2. Ice Permeability**

155 The descriptions of processes occurring within each of the first three stages of
156 seasonal pond evolution indicate that changes in the availability of meltwater outflow
157 pathways are expected to trigger the variations in pond coverage observed. These outflow
158 pathways can be grouped into two types; porosity in the ice through which meltwater can
159 percolate and macroscopic flaws to which meltwater is transported by horizontal flow

over the ice surface. A range of macroscopic flaws, including seal breathing holes [Holt and Digby, 1985], cracks [Eicken et al., 2002], and the edge of floes [Fetterer and Untersteiner, 1998], have been noted to drain substantial amounts of meltwater, particularly early in the melt season. Percolation through porosity in the ice has been observed by tracer and bail hole experiments, and is expected to occur at widely varying rates throughout the melt season [Eicken et al., 2002]. The relative importance of the two outflow pathways to the meltwater budget is, at best, qualitatively known.

An increase in brine volume, and therefore porosity, in warming ice is expected to bring about percolation as the ice pore structure becomes connective. The resulting permeability transition with rising temperature has been cited as a potentially controlling mechanism of meltwater balance responsible for pond drainage in stage II [Golden et al., 2001; Eicken et al., 2002]. This permeability transition has been explored theoretically by the application of percolation theory [Golden et al., 1998] and continuum models [Petrich et al., 2006] and experimentally through observations of Antarctic ice flooding [Golden, 2001], the use of X-ray computed tomography [Pringle et al., 2009; Golden et al., 2007], and field tests with a bail hole technique similar to that used in terrestrial hydrology [Frietag and Eicken, 2003; Eicken et al., 2004; Kawamura et al., 2006]. Percolation theory predicts that the connectivity of brine-filled pores will increase very rapidly when porosity nears a critical fraction. Adapting theory used in the study of compressed powders to the specific geometry of sea ice has produced predictions of this threshold at 5% brine volume [Golden et al., 1998], consistent with observations [Ono and Kasai, 1985]. Using well known relationships between temperature, salinity, and brine volume [Frankenstein and Garner, 1967], however, it can be shown that a brine volume of 5% is

183 reached in typical FYI well before melt ponds begin to form; suggesting that the bulk of
184 the ice beneath the ponds is substantially permeable. Measurements of the Darcian
185 permeability constant beneath ponds on summer ice of between 10^{-9} and 10^{-11} support
186 this [Frietag and Eicken, 2003]. Early summer observations of widespread pond
187 formation above sea level, however, require that the ice remain relatively impermeable to
188 downward percolation, with permeability constant substantially less than 10^{-12} [Frietag
189 and Eicken, 2003], well after the brine volume has passed 5%.

190 The discrepancy is believed to lie in the uppermost layers of ice [Eicken et al.,
191 2002], in which direct measures of permeability, such as the bail hole tests, are not
192 possible, and where several assumptions of the percolation model may not hold. This
193 portion of FYI, which is typically of granular structure, is expected to have lower pore
194 connectivity than the columnar ice below, resulting in a higher porosity threshold for
195 percolation and lower permeability in general [Golden, 2001]. Also, a layer of
196 superimposed fresh ice with lower expected porosity that forms when snowmelt refreezes
197 on the ice surface may effectively seal the ice surface. Though most references identify
198 superimposed ice as a discrete layer composed entirely of refrozen snowmelt that forms
199 on top of the existing sea ice [e.g. Granskog et al., 2006], at least one describes
200 superimposed ice extending into the uppermost part of the sea ice [Freitag and Eicken,
201 2003]. Under the latter definition, superimposed ice may consist of a mixture of sea ice
202 and refrozen meltwater formed when snowmelt percolates into the pores of the sea ice
203 and refreezes. We observed both phenomena and note that the two appear to play
204 different roles, sufficiently unique to merit clear separation. We therefore refer to the

second mechanism, in which the 'superimposed ice' is formed within the matrix of the sea ice, as the formation of *interposed ice* in this paper.

3. Methods

3.1. Observations

Field studies of melt ponds were conducted on seasonal, landfast ice in northern Alaska during the summer melt seasons of 2008, 2009, and 2010, with particular focus in 2009. Study periods ran each year from late May, prior to the onset of ponding, through mid to late June, when the ice became unsafe to work on. During this time, all of the snow and between a third and one half of the ice volume melted. Our key variables, pond coverage and albedo, were measured along transect lines daily for the duration of the experiments during all three years. Meanwhile, a wide range of other measurements were taken in 2009 and 2010 to monitor phenomena identified as potentially important factors driving melt pond development.

Measurements were collected at repeatedly visited sites just north of Barrow, AK, approximately 1 km offshore from Niksiuraq on landfast ice in the Chukchi sea, near 71.366 N, 156.542 W. The exact location of the observation sites was selected each year to represent level, snow covered FYI. Close inspection showed that the area within sites ranged from pieces of absolutely flat, un-deformed ice, to ice which had finger-rafted early in the growth season, to a very lightly rubbled field of 5-10 cm thick blocks. The general character of the sites is considered typical of undeformed first year pack ice [Shapiro and Barnes, 1991]. One measurement site was monitored in 2008 and 2010 while two sites, about 1 km apart were monitored in 2009. The 2009 sites represented

228 slightly different ice types, with the North site including some lightly rubbled ice while
229 the South site was very flat. The North site was also, fortuitously, located in a relatively
230 small hydraulic basin which enabled us to better constrain meltwater balance there.
231 Though the arrangement of the sites varied, Figure 3 shows a schematic of a composite
232 site illustrating key features of the experimental setup. An area approximately 100 m x
233 200 m in size was marked off for non-invasive observation; principally by scanning with
234 a terrestrial LiDAR scanner (TLS). This area was not entered during the campaign. Along
235 one 200 m edge of this area a transect line was set up for measurements which required
236 human presence. Surrounding the non-invasive observation area are platforms, stakes,
237 and reflectors anchored into the ice for use during TLS data collection and registration.
238 The size of the observation sites was selected to be 4-5 times the characteristic length of
239 the snow drifts and melt ponds to collect a representative sample of the surface
240 conditions.

241 The 200 m transect, marked at the top of Figure 3, was set up with one side
242 designated for travel, and the opposite left pristine for measurements. Travel along the
243 transect was limited to the four foot-travel passes per day required to gather the
244 measurements, and had no apparent effect on the surface evolution of the pristine side. A
245 typical suite of daily measurements taken along the transect line included wavelength
246 integrated albedos from 300-3000 nm measured every 2.5 m with a Kipp and Zonen
247 albedometer, spectral albedos from 350-2500 nm taken every 5 m with an Analytical
248 Spectral Devices FS3, and snow or pond depths taken every 0.5 m with a Snow-Hydro
249 automatic snow depth probe. Albedo measurements were collected by mounting the
250 sensor on a 1.5 m long arm and positioning it ~1 m above the snow surface to minimize

shadowing [Grenfell and Perovich, 2004]. The surface conditions along the line were photographed every 2.5 m and the surface type was characterized to 0.1 m resolution using a tape measure laid along the transect. Also along the transects, ice thickness was measured prior to the onset of melt using an EM-31 electromagnetic induction sensor [Eicken et al., 2001] and at the end of the experiment using a thickness tape in holes drilled every meter along the line. Snow density cores were taken just away from the line to represent the range of snow pack depths present without disturbing other measurements. Depths were recorded and cores were weighed in the lab for density calculation.

Non-invasive study areas were present in 2009 and 2010. In 2009, these areas were repeatedly photographed from a kite- or airplane-borne camera as the melt season progressed, whenever cloud conditions permitted. Kite-borne images were captured with a Canon Powershot SD 890 triggered by an FM remote control servo, suspended below the kite line by a 4 point harness. Airplane based images were captured with a Nikon D70 SLR camera mounted in a custom cradle and triggered to take images with a remote intervalometer. Image mosaics were constructed using PTGui and Autopano Pro software.

In both 2009 and 2010, the non-invasive study areas were scanned with a TLS approximately every other day, as wind, fog, and precipitation permitted, to generate detailed maps of the surface topography. The scan data was captured with a Riegl LMZ-420i scanning unit using a 1500 nm laser mounted on a tripod ~2.5 m above the ice surface. The tripod was erected on specially built platforms, which were frozen into the ice in early April. This eliminated scanner movement relative to the melting ice during

scans; a significant problem in earlier attempts. The scans captured from each platform were registered to one another using 10 fixed cylindrical retro-reflectors as registration points to create a full point cloud of the site surface using Riscan Pro software. The standard deviation of tiepoints calculated during registration of scans from a given day is typically less than 5 mm, but as high as 10 mm on particularly windy days (>10 m/s) when stabilizing the scanner became difficult. Artifacts caused by laser reflection from melt pond surfaces, fog, or precipitation, are removed in Quick Terrain Modeler and Matlab software. Surface measurement density is highly dependent on proximity to the scanner and slope aspect of the surface. The lowest point densities are about 150 points/m^2, near the center of the study area. Melt ponds generally do not reflect the near infrared laser used by the scanner strongly enough to register a direct return. Tying the ring of lowest return points collected at the rim of the pond, however, allows satisfactory representation of the pond surface level when a Digital Elevation Model (DEM) is created from the point cloud.

Translational ice movement prevented the use of DGPS reflector locations for co-registration of point clouds taken on different days. Instead, we left the reflectors frozen in place for the duration of the experiment and registered all scans to the reflector array as if it were static. The use of this ice-based reference assumed there was very minimal deformation in the ice within the reflector array. Standard deviation of registration between daily reflector position arrays and the 'true' position array does not exceed 1.5 cm, indicating that this was a reasonable assumption. The slight deformation which did occur was found to accumulate gradually and deviation between consecutive day's reflector arrays (<7 mm) was near the accuracy the scanner. Deformation in the reflector

297 array did result in a slight tilting of the registered scans with respect to the X-Y plane
298 over the study duration, by as much a 2.5 cm vertical per 100 m horizontal. To avoid the
299 unrealistic result of slightly tilted water surfaces, we chose to correct the projection of the
300 data onto the coordinate system using the inclinometer data collected by the scanner at
301 the expense of a slight loss in absolute accuracy.

302 Surface elevations collected by the scanner compare very well with manual laser
303 survey profiles and fixed ablation stake readings. Average bias compared to these
304 methods is below 1 cm and standard deviation of individual points is 2-3cm, due mostly
305 to scatter in individual scan returns and differences in the exact sample locations between
306 methods. With all errors and corrections in consideration, the comparison of consecutive
307 day's average surface height measurements at the centimeter level remains reasonable.
308 Total surface height location error compounded over the melt season is less than 5cm,
309 which, given total ablation of about 50 cm, translates to under 10% error.

310 As part of our efforts to monitor the movement of meltwater into and through the
311 ice, 10 cm diameter ice cores were taken every 2-3 days from which temperature,
312 salinity, and stable isotope ratios were measured. Holes created during coring have been
313 observed to drain substantial amounts of meltwater, significantly altering the area melt
314 ponds. Because of this, the ice coring site was selected each year more than a kilometer
315 away from the primary observation site in ice of the same character. Cores used for
316 salinity and isotope measurements were cut into 5 cm sections and bagged immediately
317 after extraction to minimize brine drainage. Temperatures were measured out of direct
318 sunlight at the center of a second adjacent core by inserting a temperature probe into
319 holes drilled into the core within a few minutes of extraction. Samples collected for

320 salinity and isotope measurement were melted in double sealed bags at room temperature.
321 A sample from the well mixed bag was taken in a glass vial for later isotope analysis,
322 then salinity measurements were made with a YSI 30 conductivity probe having stated
323 measurement error of 1% of bulk salinity. Isotope samples were sent to the University of
324 Utah Stable Isotope Ratio Facility for Environmental Research for measurement on a
325 PICARRO Wavelength Scanned Cavity Ring-Down Spectrometer. Standard uncertainty
326 determined from laboratory standard samples is 1.6 $\delta\,^{2}H$ and 0.1 $\delta\,^{18}O$.

327 Apart from the repeated measurements at the study sites, a number of other
328 measurements were made or are available from nearby projects, including bottom melt
329 rates and temperature profiles in the ice from the Barrow Ice Observatory mass balance
330 site located adjacent to our site and radiation measurements from the DOE ARM site 4
331 km away.

332

333 **3.2. Calculating Meltwater Balance**

334 LiDAR surface height data, reported in reference to an X-Y plane defined within
335 the ice, provided a means to track the loss of meltwater from the ice surface. The surface
336 height of a location represents the sum of the thicknesses of ice, snow, and liquid water
337 present above the reference plane; $h_{total} = h_{ice} + h_{snow} + h_{water}$. Using the average
338 thicknesses and density of each phase, we calculate the total mass of water in snow, ice,
339 and liquid forms above the reference plane according to equation (1).

340 $$m_{water} = A_p(\rho_{ice}\overline{h}_{pondedice} + \rho_{water}\overline{h}_{water}) + (1 - A_p)(\overline{\rho}_{snow}\overline{h}_{snow} + \rho_{ice}\overline{h}_{bareice}) \qquad (1)$$

341 where $\rho_{ice} = 900 kg/m^3$, $\rho_{water} = 1000 kg/m^3$, and $\overline{\rho}_{snow}$ is the average snow density measured on
342 or nearest the scan date, A_p is the pond coverage fraction, and $\overline{h}_{snow}$ and $\overline{h}_{water}$ are the

343 average snow thickness and average pond depth. Repeatedly entering the LiDAR field to
344 measure snow and water depth would disturb pond evolution, so average snow and
345 meltwater depth are estimated based on 400 daily measurements taken along the adjacent
346 transect line. Average ice thickness above the reference plane is calculated separately for
347 ponded and unponded surfaces as the difference between the average surface height and
348 the average snow or water depths so that $\overline{h}_{pondedice} = \overline{h}_{pondsurface} - \overline{h}_{water}$ and
349 $\overline{h}_{bareice} = \overline{h}_{baresurface} - \overline{h}_{snow}$. Pond locations are determined directly from the LiDAR scans,
350 as ponded areas produce no return. The generality of using the snow and pond depth
351 measurements from the transect to represent the scan area was tested twice by measuring
352 5,000+ depths in the area adjacent to the transect. Both times, average depths from the
353 larger sample were consistent with those found along the transect within 1.5 cm. The
354 'snow' in measurements of $\overline{h}_{snow}$ and $\overline{\rho}_{snow}$ included the surface scattering layer of
355 deteriorating ice crystals after actual snow melted away.

356 The total amount of meltwater lost from the ice surface is calculated by
357 subtracting the mass of water above the reference plane on the date of interest from the
358 amount present at the start of the melt season.

359 $$\Delta m_{water} = m_{water}(0) - m_{water}(t) \quad (2)$$

360 During the 2009 experiment, a special effort was made to directly measure melt
361 water flow down macroscopic flaws, such as cracks and seal holes. The meltwater flow
362 rate down each flaw was calculated by measuring the profile and flow velocity of
363 channels which fed the draining hole. Depth was profiled every 10 cm across the
364 channels and flow velocities were calculated by placing a floating object in the water and
365 timing its movement along a measured path with a stopwatch. The velocity was measured

366 several times, midstream as well as closer to the edges and averaged. Flow, Q, was then
367 calculated as in (3).

368 $$Q = 0.9vA \qquad (3)$$

369 where A is the cross sectional area of the stream, v is the flow velocity averaged over
370 several measurements, and 0.9 is a simple correction factor relating average velocity to
371 surface velocity for flow over a smooth streambed [Rantz et al., 2005].

372 Both the total flow rate into the holes, and the total water drainage calculated
373 from the LiDAR are converted to units of water depth for inter-comparison by dividing
374 the volumetric flow rate $\dot{Q}$ by the area measured.

375 $$\Delta h_{water} = \frac{\dot{Q}}{A_{measurement}} \qquad (4)$$

376 The 2009 North site, situated on a pan of ice surrounded by a low ridge, presented
377 an opportunity to measure outflow within a closed basin. The drainage basin, shown in an
378 aerial view in Figure 4, was roughly 1.3x1.7 km in size, or 2.29km^2 in area via GPS
379 outline. Because of the basin size and the large number of holes, total flow rate could not
380 be measured directly at all of the holes every day. Instead, total flow was calculated by
381 systematically locating and measuring the flow down all holes in the drainage basin at
382 two points in the melt season, when aerial photos were available to aid the efforts, then
383 extrapolating the flow on other days. Data needed to extrapolate from the baseline flow
384 were gathered by repeated measurements of flow rate at a subsample of the holes, and
385 monitoring a subset of the basin area for development of new holes.

386 Twenty-nine holes were cataloged in a basin wide survey on 8 June (shown on
387 Figure 4), while forty-six holes were cataloged another basin-wide survey on 10 June.

Total water drainage rate from the basin on these days was calculated at 1.56 m^3/s and 0.73 m^3/s respectively; the equivalent to 5.9 cm and 2.8 cm of water loss per day, distributed over the entire surface. As the melt season progressed, the density of holes in the sub sampled 400 m x 600 m area increased, while the flow rate down each of the monitored holes decreased. Total flow was calculated by assuming that the flow rate at all of the holes that existed during the baseline surveys followed the trends observed at the sustained monitoring holes, and that new holes appeared over the entire basin after the baseline surveys with the same density and flow rate as in the sub-sampled area.

The error in this set of extrapolations is difficult to quantify, but constrained by several known points. First, there was no flow down holes prior to 7 June 2009 because ground and aerial observations showed that holes did not yet exist. Second, flow was directly measured at all of the holes on 8 June 2009 and 10 June 2009. Third, by 15 June 2009 flow was near zero again because flow down all of the holes had ceased to be measurable. These data points are sufficient to establish the conclusions of the following sections. The extrapolations should be viewed as a best estimate for the intervening times.

4. Results and Analysis

4.1. Pond Evolution, Albedo, and Energy

Pond coverage and albedo varied tremendously during the course of each field campaign. In contrast to the observations compiled in Figure 1 from different locations and ice types, however, they followed a similar seasonal evolution each year. A plot of pond coverage vs. date, monitored along our transect lines during each of the three years

411 can be found in Figure 5a. Shifting the time scale to remove variation in the onset date of
412 pond formation (Figure 5b) highlights the similarities in the pattern of pond evolution
413 from year to year. On this plot we can identify the first three general stages of pond
414 coverage development described above. Once pond formation began, coverage rapidly
415 increased for 4-6 days to a peak at more than 50% (Stage I), then coverage declined for
416 the next 5-7 days to a minimum (Stage II). After this, coverage gradually increased for
417 the remainder of our time on the ice (Stage III). The dramatic change in the icescape
418 caused by the rapid dynamics of pond evolution is captured by a series of dated
419 composite aerial photos and LiDAR scans presented Figure 6.

420 The changes in integrated shortwave albedo caused by shifts in pond coverage
421 were quite significant. Spatially averaged albedo, calculated from measurements along
422 the transect lines, is plotted in Figure 5c. Prior to pond formation, when the ice surface is
423 snow covered, albedo is relatively stable. Albedo varies between ~0.7 and ~0.8
424 depending on the age and surface temperature of the snow. As snow melts, exposing bare
425 ice and forming melt ponds, albedo drops significantly and begins to show greater
426 variability. We note that albedo follows a trend inverse to that of pond coverage. Plotting
427 albedo vs. pond coverage in Figure 5d illustrates the strength of this correlation and helps
428 to confirm that pond coverage is the primary driver of albedo changes on melting ice
429 [Grenfell and Perovich, 2004].

430 Despite the short duration of enhanced pond coverage during stage I and II of
431 pond evolution, timing of these stages near peak annual insolation results in a large
432 impact on the surface energy balance. Insolation data, collected at the DOE Atmospheric
433 Radiation Measurement site about 4 km away, show that average solar input during the

434 study periods was 254 W/m^2, with a standard deviation between daily values of 57 W/m^2
435 (Table 1). The observed spatially averaged albedo range after pond formation of ~0.25 to
436 ~0.60 therefore translates to a range in absorbed shortwave flux of around 90 W/m^2;
437 enough energy to melt about 2.3 cm of ice per day. Even moderate changes in the
438 duration of peak pond coverage could therefore have significant impacts on overall ice
439 mass balance. Though the duration of peak pond coverage did not exhibit high variability
440 during our three year program, spiking above 45% for only 2-4 days each year, other
441 studies on undeformed FYI have observed much longer stage I duration, with early
442 season pond coverage peaking in excess of 45 % for 10-13 days [Scharien and Yackel,
443 2005; Eicken et al., 2004].
444
445 **4.2. A Brief Comparison of Pond Observations to Model Parameterizations**
446 Two predictions of pond coverage, calculated based on published GCM
447 parameterizations, are plotted with our 2009 pond coverage observations in Figure 7. The
448 first, based on the CCSM CICE 4.0 parameterization [Hunke and Lipscomb, 2010],
449 calculates pond coverage from meltwater generation rate, retaining 10% of the meltwater
450 created and distributing it into ponds having a linear depth to area fraction
451 relationship $h_p = 0.8 f_p$. The melt water generation rate used to force the parameterization
452 was calculated from snow and ice melt rates observed at the ablation stakes surrounding
453 our 2009 sites. The second, based on a parameterization designed for ECHAM5
454 [Pederson et al., 2009], uses the provided relationship,
455 $f_{mp} = 0.5 * \tanh(30 d_{mp} - 2.5) + 0.5$, to relate FYI pond fraction, f_{mp}, to pond depth, d_{mp}.

456 This parameterization is forced with average pond depth measured along the two 200 m
457 transect lines.

458 Each parameterization tracks part of the melt season quite well, but miss-
459 estimates the pond fraction in another part of the melt season substantially. Compared to
460 the pond observations, both would produce errors in albedo, and therefore energy
461 balance, over this first two weeks of ponding in excess of 50 MJ/m^2. We realize that this
462 direct comparison has limited scope because the parameterizations represent all ice types
463 and because they likely behave differently outside their typical forcing environment. The
464 comparison does, however, highlight a general challenge faced by these
465 parameterizations. Both models rely on a functional relationship to convert between pond
466 depth and area fraction; CICE a linear function, and ECHAM a more complex function.
467 The CICE model also relies on a functional relationship to convert between meltwater
468 volume produced and meltwater volume retained in ponds. Our observations of these
469 relationships (Figure 8a and b) show that, due to substantial topographic evolution and
470 dramatic changes in meltwater balance during the melt season, neither of these
471 relationships can be represented by a function. For example, in Figure 8a, a pond depth of
472 0.07 m has three different corresponding pond fractions ranging from 0.05 to over 0.45.
473 Improving these parameterizations will require incorporating an understanding of how
474 these functional relationships also change with time during the melt season. A better
475 solution still would be to relate meltwater controls to ice properties already being tracked
476 in the GCM's.
477

478 **4.3. Mechanisms of Pond Evolution**

A principal goal of this work is to improve understanding of the mechanisms which drive pond evolution. Two direct controls of pond coverage, meltwater balance and surface topography, provide a structure around which to organize the presentation of our results.

4.3.1. Topographic Control of Pond Coverage

The LiDAR surface elevation models enabled us to observe ice topography in great detail prior to melt and as it evolved through the melt season. Pre-melt ice topography was expected to play a key role in determining the location and peak coverage of melt ponds by controlling the distribution of meltwater. Most of the surface relief at the sites, however, was created by snow atop the ice, rather than the ice itself. The importance of the combined snow and ice relief was investigated by comparing pond locations throughout the melt season with the pre-melt snow topography at those locations. Each day that LiDAR scans were taken, the vertices of a 10 cm grid over the study site were denoted as either ponded or un-ponded. The scanner's 1500 nm laser generally produces no return from liquid water so the surface state within each cell was determined based on whether a return was received from within the cell (un-ponded) or not (ponded). The average pre-melt surface height in each ponded grid cell was then retrieved from scan data taken a week prior to pond formation. The surface height distribution of ponded areas is divided by the total pre-melt height distribution to calculate the fraction of pre-melt surface of a given height that is ponded on the date of interest. These distributions are plotted in Figure 9a. The high fraction of areas with low pre-melt surface height pond covered during stage I (6 and 7 June) confirms that pre-melt

surface height, dictated largely by snow dune formation, is a strong control of whether ponds will form at a given location. The use of individual LiDAR returns and slight surface height differences between unconnected ponds across the site induce 2-3 centimeters of scatter in the apparent fill line, but by peak pond coverage on 7 June, 95% of the points which had a pre-melt surface height of less than 0.35 m are pond covered, while only 17% of those which had a height over 0.39 m are ponded. Furthermore, the percentage of the cumulative pre-melt surface height distribution (dashed black line) that was below the fill level (54% below 0.38 m), is in close agreement with the pond coverage of 52% on 7 Jun. The effect of pre-melt topography during stage I is further evident visually in Figure 10, which shows a height-colored image of the pre-melt season surface, and an adjacent height-colored image of just those areas which were pond covered on 7 June.

As the pond coverage drops during stage II (8-13 June 2009), the orderly filling of points with the lowest pre-melt surface height is not strictly preserved. Pond coverage in areas where pre-melt surface height was just below the fill line drops first; but not to zero. The very lowest pre-melt areas continue to have the highest pond coverage, but not nearly 100%. Figure 9a shows that by 13 June, when pond coverage reaches its minimum, most of the pre-melt height categories below the fill line still have at about 5% of their area pond covered. Cumulative distributions of the pre-melt surface height in ponded areas, presented in Figure 9b show that the distribution of pre-melt surface heights in ponded areas doesn't change much as ponds drain. Essentially, the areas which remain pond covered for the rest of the melt season are subset of those areas which were ponded at peak coverage, but there is not a strict preference for the areas of lowest initial

surface height. That points of initial height below the fill-level appear to have similar likelihood of remaining ponded regardless of pre-melt height suggests that another control of topography, which operates only in the ponded covered areas and without respect to initial surface height, enhances relief during stage II. Two such controls appear significant during stage II; the presence of sediment in the ice, and flow toward drainage points in meltwater channels. Both enhanced ablation in pond bottoms and appeared to be spatially uncorrelated to initial surface height. Qualitative observations suggest that both processes can locally enhance pond bottom ablation rates by 50-100%, and that the pond locations on 13 June were strongly correlated to these processes. Determining the importance of these factors in creating the below sea level pond depressions that remain ponds after stage II will require further study.

During stage III, abundant outflow paths maintain pond surfaces near sea level. Increases in pond area occur only when the surface height of new areas drops below sea level. Two potential mechanisms were identified that increased the area where the ice surface is below sea level; lateral melt at the walls of the ponds and losses in overall ice freeboard occurring as ice thinned and buoyancy force declined. The locations where ponds grew during stage III at the 2009 N site, highlighted in blue in Figure 11a, suggest that freeboard decline caused most of the pond growth in stage III. The horizontal rate of growth at some pond edges, working out to much as 1 m per day, is much higher than lateral heat transfer would be expected to cause. The pattern of growth also shows no preference for pond walls that faced into the prevailing wind, where waves would be expected enhance lateral heat transfer. Growth did appear, however, to be concentrated in areas where surface height was low at the start of stage III (compare Figure 11a, showing

548 where ponds grew, to Figure 11b showing areas within 7 cm of sea level on 13 June).
549 Cumulative distributions of all surface heights at the start of stage III and of just the areas
550 where ponds grew during stage III can be seen in Figure 12. Approximately 85% of the
551 area where ponds grew was within 7 cm of sea level at the start of stage III compared to
552 only 20% of all unponded surfaces at that time.

553 During the same part of stage III, the LiDAR data show that the average ice
554 freeboard declined about 4 cm; roughly what is expected from buoyancy loss due to the
555 ~35 cm ice thinning observed during this period. Even allowing for 2 cm of scatter in
556 individual LiDAR measurements widening the height distribution, some areas which
557 ponded were slightly higher than would have been flooded if topography was simply
558 preserved. Still, ponds formed almost entirely on the areas closest to sea level. Combined
559 with the observation that areas of ice with very low freeboard become darker and melt at
560 higher rates as their surface scattering layer thins, it seems reasonable to conclude that the
561 freeboard decline controlled pond growth and resulted in flooding areas 2-3 cm higher
562 that would have be flooded if topography was simply preserved.

563 While freeboard loss appears to dominate pond growth during the first 10 days of
564 stage III, roughly half of the starting ice mass remained when we left the ice. In order for
565 ice freeboard to continue to be the predominant mechanism of pond growth during later
566 melt, there must be remain large areas of ice near freeboard that will flood with
567 incremental losses of freeboard. Because of preferential melt in the ponds, however, we
568 would expect ponds to sink into ever deeper wells where the effects of freeboard loss
569 would be damped. Lateral melt might take over as the predominant growth mechanism.
570 To examine the extent to which this occurred during the first part of the melt season, we

plot cumulative distributions of the surface height for scans taken during stage III, in relation to sea level at the time of each scan (Figure 13). The amount of ice within 5 cm of freeboard changes very little during our observations and still covers 10% of the total area on 23 June, which suggests that freeboard loss continued to control pond growth after our departure.

4.3.2. Water Balance Control of Pond Coverage

While topography controlled pond location and meltwater distribution, qualitative observations collected during our study suggested that changes in the availability of meltwater outflow pathways dictate the timing of stages in seasonal pond evolution. During the rapid rise in pond coverage of stage I, pond surfaces were well above sea level, indicating that outflow pathways were very limited. The first noted appearance of macroscopic holes draining meltwater from the surface each year coincided with the first day of pond coverage decline in stage II. Combined with evidence of rapidly dropping pond levels, the appearance of the holes appeared to significantly enhance outflow. Flow slowed at the macroscopic holes as pond level approached sea level, ceasing entirely as the ponds reached a minimum coverage at the end of stage II. Thereafter, no meltwater flow could be detected at the macroscopic holes, though ablation continued at several centimeters per day. Pond levels remained fixed to sea level, indicating that meltwater was now leaving the surface by another means; presumably percolation through the ice.

Calculations of meltwater loss derived from the LiDAR surface models provide an opportunity to test these observations. The results of this analysis, conducted on the North observation site in 2009, are plotted in green on Figure 14, along with dashed

marker lines denoting the three stages of pond evolution. The data show that the total amount of meltwater lost from the surface of the ice is near zero for several days after the melt ponds form. Though snow and ice are being converted to liquid water, there is very little, if any, outflow during stage I. All outflow pathways appear to be shut down.

Meltwater loss begins abruptly on 8 June, coinciding with the start of pond coverage decline (stage II) and the first observations of macroscopic flaws draining meltwater in the area. Though the timing of the holes' appearance suggests that the lost meltwater drains down them, we measured outflow at the holes to determine whether percolation through the ice was also active. The 2009 North observation site provided an opportune site for this study because it was located within a closed hydraulic basin defined by a low ridge. Combined with the lack of significant precipitation during this time (<1 cm), and minimal expected evaporation (rH >90%, T=~0°C), the features of this site allow us to make a direct comparison of the flow measured at the holes within the basin, plotted on Figure 14 in blue, to the LiDAR-derived total meltwater loss. The two curves track one another closely during stage II, indicating that the vast majority of the meltwater lost from the surface of the ice is accounted for by flow down the macroscopic drainage holes. The ice, therefore, remained largely impermeable to percolation during stage II and the reduction in pond coverage was controlled by horizontal transport of meltwater over the ice surface to macroscopic flaws.

As we move into stage III, however, and the ponds drain down to sea level, the flow measured at the holes no longer accounts for the meltwater being lost, and soon stops altogether. The meltwater lost instead must drain by percolation through the ice. We therefore conclude that the ice underwent a rapid permeability transition over the 2-3

617 days centered on 13 June and percolation through the ice is the primary means of
618 meltwater loss in stage III. Though not responsible for the pond drainage, percolation was
619 responsible for fixing pond height to sea level in late melt.
620
621 **4.4. Interactions of Meltwater with Ice**
622 The analysis of meltwater flows confirms the power of hydraulic controls on the
623 pond evolution and provides insight into relative importance and the timing of transitions
624 between outflow mechanisms. This information enables the identification and further
625 exploration of the mechanisms of ice and meltwater interaction which caused the
626 appearance of drainage flaws and the observed permeability transition.
627
628 **4.4.1. The Formation of Flaws from Brine Channels**
629 Each year of our study, the macroscopic flaws, implicated as the cause of pond
630 coverage decline in stage II, were not observed until the first day of melt pond decline,
631 and seemed to spontaneously arise between daily visits to the site. During 2009,
632 sequential daily aerial photos presented additional evidence of the holes' sudden
633 appearance. The first holes observed from the ground were readily visible in aerial
634 photographs taken on 8 June, but absent in photos taken the day before, prompting us to
635 explore their origin. Seals were present at some of the holes, suggesting that they were
636 breathing holes kept open through the winter, as others have concluded when observing
637 similar drainage features [Barber and Yackel, 1999; Holt and Digby, 1985]. The seal
638 holes are even known to have a protective dome of ice and snow through the winter
639 which the seals often remove in order to haul out for basking behavior necessary to molt

640 at this time of year [Brendan Kelly, personal communication], potentially explaining a
641 sudden appearance.

642 Indeed some of the very first holes noted were likely seal holes, as seals have
643 been documented in previous years maintaining breathing holes through the ice within
644 the study area [Kelly, 1996]. Over the next several days, however, the number of holes
645 visible in aerial photographs (e.g. Figure 15a) and confirmed from ground observations
646 grew rapidly, to numbers which greatly exceeded the expected density of seal breathing
647 holes [Gilford Mongoyak, Inupiat hunter, personal communication]. Throughout stage II,
648 while meltwater level in the ponds remained above sea level, holes appeared each day
649 where they had not been noted the previous day. New holes widened in proportion to
650 their flow rate, reaching diameters as large as 2 m, but more typically 0.5 m. We
651 observed similar widening with manmade holes created when cores were taken from
652 ponds at our coring sites. More interesting, however, was the observation that the
653 smallest holes found were under 5 cm in diameter. The small size, combined with the
654 shear number of holes found, over 100 per km^2 by 16 June, indicated the origin of the
655 vast majority of the holes was unlikely to have been related to the seals.

656 Instead, organized brine drainage channels, which have long been known to form
657 during ice growth to reject brine [Lake and Lewis, 1970], were identified as a potential
658 origin of the majority of the holes. These features were observed preferentially melting at
659 the surface in many places, (Figure 15d) and evolving into tiny connective holes (Figure
660 15e). We hypothesized that as ice temperatures increased the brine volume in these
661 channels would increase, until they became connected from the surface to the ocean,
662 allowing meltwater to begin flowing down them. Once flow began, heat transfer from the

663 moving water rapidly widened the hole, just as it did for holes drilled in the bottom of a
664 pond at our coring site (Figure 15f, 15g). Several of the non-connective brine drainage
665 channels visible at the surface were removed in ice cores to observe the development
666 prior to connectivity. In these cores, we were easily able to identify the bottom of the
667 channels due to enhanced algal growth (Figure 15c). Horizontally sectioning the cores in
668 the field allowed us to follow the open, 0.25-0.75 cm diameter brine drainage holes
669 (Figure 15b) most of the way through the ice. The exception was a portion about 0.65 to
670 0.85 m below the surface in 1.05 m thick ice which corresponded with the coldest part of
671 the ice (T= -0.9°C) and where the channel could not definitively be seen. We
672 hypothesized that these non-connective channels had actually become plugged with
673 refreezing meltwater, a theory that we explore in much greater detail below.
674
675 **4.4.2 The Permeability Transition**
676 Though flaws forming from brine channels controlled meltwater drainage in stage
677 II, the meltwater data show that the predominant mode of meltwater loss transitioned to
678 percolation during the beginning of stage III. The rapidly increasing volume of water lost
679 to percolation during the transition, despite dropping hydraulic head, indicates that the
680 increase in ice permeability was rather abrupt. Mechanisms suggested for causing such a
681 transition in ice permeability include reaching a porosity threshold above which pore
682 connectivity rapidly increases (percolation theory) [Golden, 2001; Fetter and
683 Untersteiner, 1998], the destruction of a surface layer of impermeable superimposed ice
684 formed during snowmelt [Eicken et al., 2004], and the destruction of a layer of ice in
685 which the pores have been plugged by the formation of interposed fresh ice [Freitag and

686 Eicken, 2003]. Our knowledge of the timing of the permeability transition, combined
687 with simultaneous measurements of ice properties, provides an opportunity to examine
688 each of these mechanisms.

689 One application of percolation theory to ice makes a clear prediction that the ice
690 should undergo a permeability transition at about 5% brine volume [Golden, 2001]. Ice
691 porosity, p, presumed to be equivalent to the brine volume, was calculated in our
692 experiment according to (5), using salinity and temperature profiles collected from ice
693 cores and embedded thermistor strings [Frankenstein and Garner, 1967].

694 $$p = S\left(0.0532 - \frac{4.919}{T}\right) \quad (5)$$

695 where S is salinity in psu, T = temperature in °C, and p = % porosity.

696 Dated vertical profiles of calculated porosity from prior to the onset of ponding
697 can be found in Figure 16b. Comparing the data to a 5% brine volume percolation
698 threshold (marked as a vertical line) shows that the entire profile of the ice exceeded the
699 percolation threshold during the first weeks of May, about six weeks prior to the
700 observed onset of meltwater percolation, and a month prior to the initial formation of
701 ponds. Ice salinity profiles, shown in figure 16a, begin to show freshening in the
702 uppermost layers of the ice at this time, indicating the start of brine gravity drainage and
703 the onset of ice permeability, as expected from theory. Because brine movement occurs
704 even in the upper, granular, ice layers, which are believed to have a higher percolation
705 threshold due to less organized brine inclusions structure [Golden, 1998], the entire ice
706 column has passed through its porosity-based percolation threshold. These observations
707 support the application of percolation theory to predict a sea ice permeability transition
708 based on pore connectivity. Timing clearly indicates, however, that the initial,

709 temperature dependent increase of porosity through the percolation threshold is not the
710 mechanism responsible for the onset of meltwater percolation through the ice.
711 The formation of either superimposed or interposed fresh ice could provide a
712 means to prevent percolation through an ice cover with high bulk porosity. Superimposed
713 ice, defined here as a discrete layer of refrozen snowmelt forming on the surface of the
714 ice, was observed extensively in all three study years. Qualitatively, the superimposed ice
715 layer was of highly variable thickness. Clearing the snow from the ice after the onset of
716 snowmelt but prior to pond formation, showed a bumpy layer of newly accreted ice
717 consistent with spatially heterogeneous percolation of meltwater through the snow. The
718 layer's thickness was highly dependent on snow depth, averaging up to 8 cm thick
719 beneath 40 cm deep snow dunes, but less than 4 cm thick and often absent entirely in
720 areas of thin snow cover which would later be the sites of melt ponds. Beneath snow
721 dunes, superimposed ice was sometimes thick enough to be identified in cores taken after
722 the onset of ponding. The extremely fresh superimposed layer typically yielded
723 substantially lower porosity, as derived from temperature- and salinity-determined brine
724 volume, than the rest of the ice; often below the 5% percolation threshold. The use of
725 brine volume as a proxy for porosity, however, may not be valid in the case of
726 superimposed ice, where substantial bubble fraction is trapped. This higher bubble
727 fraction made superimposed ice easy to identify in pond bottoms, from which the
728 superimposed ice layer was observed to separate 2-5 days after ponding in large, highly
729 porous sheets 2-4 cm thick (see image in Figure 17). We tracked the presence of this
730 layer visually in the bottoms of the melt ponds, characterizing ponds along the transects
731 as being lined with either superimposed ice or sea ice. The percentage of pond bottoms

732 free of superimposed ice in 2009 is plotted in Figure 18. Superimposed ice began to break
733 free of the pond bottoms on 5 June, and nearly all pond bottoms were free of
734 superimposed ice by 9 June, about 3 days before the permeability transition. The timing
735 of the gradual loss of superimposed ice several days earlier than the permeability
736 transition, indicates that superimposed ice removal is likely not the cause of the
737 permeability transition.

738 Another smaller basin which we monitored in 2009 helps to further demonstrate
739 this point. The basin, pictured in Figure 19, did not develop a macroscopic flaw until 11
740 June and exhibited no net loss in melt water equivalent, inferred from LiDAR, well after
741 the rest of the ice had begun draining. The pond within the basin both deepened and
742 widened until, on 11 June, it drained in a matter of hours down a macroscopic flaw which
743 formed in the bottom of the pond. By that time, all of the snow, and more than 20 cm of
744 the sea ice on the bottom of the pond had ablated, according to fixed ablation stakes
745 within the pond. The superimposed ice layer had clearly been removed, while the ice
746 remained quite impermeable. Though superimposed ice was observed to form, and may
747 or may not be impermeable, its removal did not trigger the permeability transition at the
748 start of stage III.

749 There is substantial evidence in our data supporting the notion that fresh
750 meltwater refreezes within the ice porosity to form interposed ice plugs. When meltwater
751 begins to pool on the ice surface in early June, both percolation theory and our
752 observations of brine gravity drainage suggest that connective pathways exist for water to
753 percolate into the ice. Profiles of temperature and salinity taken during melt (Figure 16c
754 and d) show desalination to increasing depths in the upper ice during stage I and II of

pond evolution, indicating that brine is being flushed from the upper pores by intruding meltwater. Deeper down, within the colder parts of the ice, however, salinity remains nearly constant, indicating that fresh meltwater is not free to flush through the colder ice, despite its high porosity. The limited penetration of meltwater during stage I and II can be confirmed by stable isotope measurements because the meltwater, composed substantially of snowmelt, is highly depleted in heavy isotopes. Vertical profiles of stable isotopes (Figure 20), taken beneath melt ponds during stage I and II, confirm the presence of substantial amounts of meteoric water up to 30 cm into the upper ice, even beneath layers of superimposed ice. In contrast, a profile collected during the permeability transition that occurs at the start of stage III no longer shows meteoric water in the upper ice and captures some light isotopes deep in the ice. Though it is unclear if the core captures meltwater which is still draining deeper into the ice from above or meltwater convecting upward from below ice melt ponds [Eicken et al., 2002], the entrainment of light isotopes on both sides of the coldest part of the ice indicates that free movement of fresh water has begun.

Despite the freshening that occurs as meltwater penetrates into the upper ice, the sea ice porosity beneath ponds, derived from bulk salinity and temperature of cores, remains well above the percolation threshold of 5%, even at the depths where we expect ice plugs must be forming. We hypothesize that this apparent contradiction of percolation theory occurs because the formation of interposed ice happens preferentially in the most critical connective pathways. As meltwater plumes percolate downward in tortuous, connective pathways, the meltwater will begin to freeze to the walls of the pores when cold ice is encountered. Given similar rates of accretion on all walls, constricted points

778 along the pathway that the water propagates would be expected to fill with ice most
779 rapidly, while larger pores may not entirely refreeze. If such constriction points exist, a
780 small volume of ice could stop percolation without significantly altering the bulk salinity
781 of the ice, as measured by our 10 cm diameter coring. By selectively blocking critical
782 connections between the pores, however, the refreezing meltwater, would alter the
783 expected relationships between bulk porosity and pore connectivity which percolation
784 theory depends upon.
785
786 **4.4.3 The Linkage Between Percolation and Flaw Formation**
787 We propose that both the formation of interposed ice and the widening of brine
788 channels are a single process dependent on the initial size of the pore into which
789 meltwater flows. When fresh melt water intrudes from above into a brine-filled pore, it
790 displaces the brine downward and comes into contact with ice which is below its freezing
791 point, causing the meltwater to freeze. The meltwater delivers heat to the inside of the
792 pore by giving off latent heat as it freezes, carrying small amounts of specific heat, and
793 frictionally dissipating even smaller amounts of kinetic flow energy. Whether a hole will
794 freeze shut and form a fresh ice plug or widen as the meltwater delivers energy depends
795 entirely on the integrated energy balance at the pore wall. Several variables affect this
796 balance, including the temperature and salinity of the ice and meltwater, the hydraulic
797 potential of the melt water, and the size of the pore. At a particular time in the melt
798 season, temperature, salinity, and hydraulic head are fixed, leaving pore size as the only
799 free variable.

Brine inclusions in the ice are expected to exist in a range of sizes and, because they are formed by two distinct mechanisms, likely have a bimodal distribution. The first mechanism of brine inclusion, entrapment of brine between interconnecting ice lamellae as the ice solid fraction increases, results in brine inclusions smaller than lamellae spacing, or typically to less than 1 mm in horizontal diameter [Perovich and Gow, 1996]. The second mechanism, gravity drainage of brine during ice growth, results in organized arborescent brine channels of diameter that can greatly exceed lamellae spacing, formed as dense brine is collected and drains along a preferred pathway from the smaller inter-lamellar inclusions [Lake and Lewis, 1970]. The few available estimates place brine channel size at 1 cm or a bit less [Golden, 2001; Lake and Lewis 1970]. The sizes of both inclusion types likely vary considerably and are dependent on temperature, however it is reasonable to expect that brine channels are roughly an order of magnitude larger than inter-lamellar inclusions. As the ice warms, we expect there would be a time at which meltwater flowing into large pores, such as well organized brine drainage channels, will enlarge the pores into a macroscopic drainage holes, while meltwater flowing into smaller pores will simply refreeze, blocking them. Simple observations confirm this general concept. Large, 10-cm diameter core holes drilled through ice in the bottoms of melt ponds are simply too large to repair and widen rapidly as meltwater whirlpools into them. Much smaller, 2-mm diameter holes, drilled in a laboratory grown block of saltwater ice, self-repaired when fresh water at 0°C was poured down them at ice temperatures of up to -0.4C.

4.4.4 Brine Channel Flow Model

We created an enthalpy based model of an idealized brine drainage channel to explore the interactions of melt water with brine channels further. Our 2D model representing a single, isolated, cylindrical brine tube consists of stacked annular cells of uniform radial thickness which retain constant volume throughout the model run. The center cells are initialized as a cylindrical tube of liquid brine, while the surrounding ice cells are initialized with temperature and salinity measured in cores taken at our site at several points during the melt season. The ice component of the model uses methods similar to those employed in a 1D ice model by Dirk [2006] tracking two primary variables, enthalpy and salinity for each gridcell, at each timestep. Enthalpy and salinity are related to secondary variables temperature and brine volume by assuming that all brine in ice-containing grid cells exists at its salinity-controlled freezing point. The concentration of the brine, S_{brine}, is calculated for a given temperature, T, using an average molecular weight of sea salt ions, $\overline{M}$ =31.41g/mol [Bromley, 1968], and the cryoscopic k_{cryo} constant of water so that:

$$S_{brine} = -T \frac{k_{cryo}}{\overline{M}} \qquad (6)$$

This enables brine volume, v_b, and the freezing point of the cell, T_f, to be determined using bulk salinity, S_{bulk}.

$$v_b = \frac{S_{bulk}}{S_{brine}} \qquad (7) \qquad T_f = S_{bulk} \frac{\overline{M}}{k_{cryo}} \qquad (8)$$

The enthalpy of each cell, H, is related to temperature and salinity according to the changes in both specific and latent heat required to reach the current brine fraction and temperature from the reference state, where H_{ref}= 334J/g at T = 0°C, fully liquid.

$$H = (1 - v_b)L - k_l T_f + v_b k_l (T - T_f) + k_s (1 - v_b)(T - T_f) \qquad (9)$$

where the first term represents the latent heat (L) required to freeze the solid fraction, the second term represents the specific heat required to cool the water to its freezing point, and the third and fourth terms represent a simple approximation for the specific heat required to cool the brine and solid fractions from the freezing point to the current temperature (T).

Radial heat transfer $\dot{H}$ is calculated at each time step according to Fourier's law of heat conduction in cylindrical coordinates,

$$\dot{H} = -kA_r \frac{dT}{dr} = -2k\pi r l \frac{dT}{dr} \qquad (10)$$

where the conductivity of the cells, k, is calculated as a weighted average of constant solid and liquid conductivities based on the brine volume $k = k_l v_b + k_s (1 - v_b)$ with

$k_l = 0.58 \frac{W}{mK}$ and $k_s = 2.0 \frac{W}{mK}$.

Heat transferred into or out of a cell is added to each cell's enthalpy value, and new temperatures, brine volumes, and conductivities and are calculated from the updated enthalpy values to begin the next time step.

Meltwater flowing into the brine channel has a fixed temperature and salinity of 0.1°C and 1.5 ppt, based on measurements of these taken in ponds which had not yet melted through to the ocean. Hydraulic head is set to 0.2 m, representative of an average head immediately prior to the formation of drainage flaws.

Fluid flow rate and heat transfer within the brine tube are approximated by two regimes based on Reynolds number of flow:

$$\mathrm{Re} = \frac{Vd}{v} \qquad (12)$$

where V is the velocity, in m/s of the flow, d is the pipe diameter, and v is the kinematic viscosity of water at 0°C. Reynolds number below 2300 indicates laminar flow, while flow with Reynolds number above 4000 is considered turbulent. The tube lengths and head height used in our model result in a turbulent Reynolds number for channel diameters greater than roughly 4 mm. Intermediate Reynolds numbers are considered transient. Flow volume in the transient state is calculated from an interpolation of the mechanisms, while heat transfer is assumed to be strictly conductive as in laminar flow.

For laminar and transient flow, volumetric flow rate is calculated using the Hagen-Poiseuille pipe flow relationship:

$$Q = \frac{\Delta P \pi r^4}{8 \mu L} \qquad (13)$$

where pressure difference is calculated from water density, gravitational constant, and hydraulic head, $\Delta P = \rho g h$, r is the tube radius, L is the tube length, and μ is the dynamic viscosity of water, $\mu = 1.787 x 10^{-3} \frac{Ns}{m^2}$.

In the turbulent regime, flow rate is calculated from conservation of energy by equating kinetic energy and frictional loss of the flow to available potential energy (*PE*) and deriving an expression for flow velocity in terms of hydraulic head and channel diameter.

$$PE = \dot{m} h g = \frac{1}{2} \dot{m} V^2 + \dot{m} g h_f \qquad (14)$$

where $\dot{m}$ is the mass flow rate of water, h is head, g is gravitational constant, V is velocity, and h_f is the frictional head loss during flow, calculated using the Darcy-Weisbach equation:

$$h_f = f\frac{l}{d}\frac{V^2}{2g} \qquad (15)$$

where l is the length of the tube, d is its diameter, V is the flow velocity, g is the gravitational constant, and f is the friction factor, which is dependant on the tube roughness and Reynolds number. Determining f explicitly requires a more detailed knowledge of the surface roughness within a brine channel than is available, however the value of f is not particularly sensitive to assumed pipe roughness or Reynolds number; varying over a range of ~0.2-0.4 for the full range of relative roughness values found in typical pipe flow problems and the range of Reynolds numbers modeled here. In order to improve the estimate of flow rate from the frictionless case, where $h_f = 0$, we assume a relatively smooth tube wall, with relative roughness = 10^{-4} and calculate f from a Moody diagram using the Reynolds number of the frictionless flow velocity $v = \sqrt{gh}$.

Substituting h_f into the (14) allows for derivation of V.

$$V = \sqrt{\frac{hg}{\frac{1}{2} + \frac{l}{2d}f}} \qquad (16)$$

Volumetric flow rate is then calculated by multiplying flow velocity by pipe cross section.

903 Radial heat transfer in the liquid is modeled by simple heat conduction for the
904 laminar and transient flow cases in the same manner as for the ice component. Enhanced
905 radial heat transfer due to mixing in the turbulent regime is calculated using a convective
906 heat transfer coefficient derived from the Dittus-Boelter correlation

907 $$\dot{H} = hA\Delta T \qquad (17)$$

908 where heat transfer coefficient $h = (k_l/d)Nu$, Nusselt number is derived from Reynolds
909 and Prandtl numbers, $Nu = 0.023\,\mathrm{Re}^{0.8}\,\mathrm{Pr}^{0.33}$, A is the area of transfer surface, and ΔT is
910 the temperature difference between the transfer surface and the fluid temperature.
911 Salinity within the ice very near (cm-scale) the channel is expected to decline
912 when fresh water begins to flow down the channel, as brine within adjacent, connected
913 pockets diffuses, convectively mixes, and becomes entrained in the freshwater flow. This
914 expected desalination was qualitatively observed by taking salinity core samples
915 immediately adjacent to developing holes. The rate of this desalination is important to the
916 model because it lowers the calculated effective heat capacity of the ice near the channel.
917 Lacking sufficient data to constrain this desalination at high resolution, we set the model
918 to run three cases. Two cases bound the result with no desalination and immediate and
919 complete desalination of the surrounding ice while a third, best-estimate case allows
920 desalination by simple diffusion. Actual desalination is most likely greater than simple
921 diffusion. In all cases, fresh ice is presumed to form on the interior of the tube if ice
922 growth occurs. Vertical heat conduction and solar energy deposition are neglected due to
923 the relatively short period of time required for a given diameter channel to either enlarge
924 or freeze. Viscous dissipation as a heat source within the channel is ignored because the
925 total potential loss of the water (head height times mass flow times gravity) distributed

926 evenly along the channel wall is at least an order of magnitude smaller than that
927 conducted from the incoming water.
928
929 **4.4.5 Model Results**
930 When run with a range of initial flaw diameters in a fixed ice profile, the model
931 results show the strong threshold behavior with respect to channel diameter expected.
932 The results of such a test are plotted in Figure 21, where the minimum channel diameter
933 is tracked over time for various starting diameters. Channels initially below a critical
934 diameter, here 1.5 cm, rapidly close when slowing meltwater flow causes a negative
935 feedback allowing thermal conduction into the ice to increasingly exceed energy delivery.
936 Only slightly above that critical diameter, the channel begins to close, but thermal
937 conduction into the ice slows as the ice is warmed, dropping below the rate of heat
938 delivery from the meltwater before the channel can be closed completely. Once energy
939 delivery exceeds conduction, the channel begins to widen and a positive feedback sets in.
940 The ratio of cross-section-dependent flow rate to circumference-dependent heat
941 conduction increases the net heat flux to the channel walls while the ice warms and
942 conduction slows. The result is a steady widening of the hole despite the increasing ice
943 volume that must be melted for a given diameter increase as the hole widens.
944 Predictions of critical channel diameter, based on ice properties collected in 2009
945 ice cores, are plotted in Figure 22 for all three desalination schemes. The results highlight
946 a decline in critical channel diameter which accelerates as the ice warms during melt. At
947 the time that drainage flaws were appearing on 8 June, the critical channel diameter
948 predictions range from 0.8-1.8 cm with the three desalination schemes. This range is in

949 quantitative agreement with the expected size of the largest organized brine drainage
950 channels, further supporting the notion that brine channels will predictably enlarge to
951 produce macroscopic flaws. After drainage flaws began to open on 8 June, predicted
952 critical channel diameter begins to drop rapidly, allowing flow through smaller and
953 smaller inclusions and suggesting that the observed permeability transition occurs
954 because the critical diameter for percolation passes below the typical porosity size. When
955 the permeability transition occurred on 13 June, predicted critical diameter is between the
956 expected size of the two brine inclusion types, leaving the relative roles of interlamellar
957 brine inclusions and smaller brine channels in causing the percolation transition unclear.
958 Expected growth of the interlamellar inclusions as the ice warms may account for part of
959 the size difference, but we also note that the observed density of brine channels in the ice,
960 at 60-120 per m^2 [Golden, 2001], is much greater than the observed density of enlarged
961 holes of roughly 100 per km^2. If the unaccounted for brine channels did not plug
962 irreversibly in early melt, percolation may proceed down these channels when the critical
963 channel diameter drops below their typical size. Clearly identifying which type of the
964 flaw causes percolation will require more precise characterization of inclusion sizes
965 during melt and in situ study. The model results, however, make clear the importance of
966 temperature dependent interactions between fresh meltwater and the porosity of the sea
967 ice in determining the availability of meltwater outflow pathways.
968
969 **5. Conclusions**
970 The summer albedo of melting Arctic sea ice is strongly affected by the fraction
971 of the surface covered by melt ponds. Melt pond coverage varies rapidly and widely over

the course of the melt season in a given place and can vary substantially from one place, or ice type, to another. Accurate albedo prediction for Arctic sea ice requires a detailed understanding the mechanisms that force changes in pond coverage. Ice surface topography and meltwater balance are found to both play key roles in melt pond evolution. Topographic relief prior to the onset of melt, caused largely by snow dunes atop undeformed FYI, determines the locations of initial pond formation while the magnitude of the surface relief controls the areal extent of meltwater distribution. The temporal evolution of melt pond coverage occurs in discrete, readily identifiable stages whose transitions are controlled by the ice temperature dependent development of meltwater outflow pathways. During the stage I, ponds form well above sea level. The ice is found to be impervious to meltwater percolation and generally free of macroscopic flaws draining meltwater, though some meltwater would be expected to run off the edge of floes in the floating pack. The rapid drainage of meltwater that occurs as pond coverage declines during stage II is predominantly due to horizontal transport of meltwater over the ice surface to macroscopic flaws. Though any large aperture through the ice may drain meltwater during this time, the vast majority of the meltwater was found to drain down holes formed from the enlargement of brine drainage channels by flowing meltwater. The formation of interposed ice within sea ice porosity blocks theoretically expected ice permeability during stage I and II of pond development. At the start of stage III, which is defined by practically unlimited outflow pathways, percolation begins abruptly. Pond level is fixed to sea level throughout this stage, while overall freeboard loss results in the steady growth of ponds by surface flooding.

994 The formation of meltwater outflow pathways that drive the stages of pond
995 development is controlled by interactions of fresh meltwater with brine inclusions. Our
996 model of meltwater intruding into a brine-filled pore shows that whether a specific pore
997 will enlarge or become plugged by refreezing meltwater is highly dependent on ice
998 temperature, salinity and the initial pore size. The distribution of pore sizes expected
999 within the ice allows this behavior to explain the observed temporal separation between
1000 the onset of macroscopic flaw formation and the onset of percolation.
1001 The key findings of this experiment mechanistically link the temporal evolution
1002 of pond coverage, and therefore ice albedo, to ice temperature and salinity. If coupled
1003 with detailed measurements of surface topography distribution and brine inclusion
1004 characteristics on other ice types, these results provide a promising path toward
1005 improving explicit handling of melt ponds within model parameterizations.
1006
1007 **Acknowledgements:** We gratefully acknowledge the loan and support of a TLS from
1008 Dave Finnegan, substantial field work contributions by Kerry Claffey, and able technical
1009 assistance of Bruce Elder. Ice core and surface elevation data used to validate and
1010 improve several findings was collected and generously made available on the Barrow Ice
1011 Observatory website by Chris Petrich, Hajo Eicken, and Matthew Druckenmiller, who
1012 also all collaborated most helpfully in the field. Logistical support was provided by the
1013 Barrow Arctic Science Consortium, particularly Gilford Mongyak, Nok Acher, Michael
1014 Donovan, and Lewis Brower. This research was funded by the National Science
1015 Foundation through Grant ARC-0454900 and fellowship support of the Dartmouth
1016 College Polar Environmental Change IGERT Program.

1017 REFERENCES

1018 Barber, D. G. and J. Yackel (1999), The physical radiative and microwave scattering characteristics of melt
1019 ponds on Arctic landfast sea ice, *Int J. Remote Sensing, 20,* 10, 2069-2090.

1020 Bromley, L. A. (1968), Heat Capacity of Sea Water Solutions. *Journal of Chemical and Engineering Data,*
1021 *13* (1), 60-62.

1022 Derksen, C., J. Piwowar and E. LeDrew (1997), Sea-Ice Melt-Pond Fraction as Determined from Low
1023 Level Aerial Photographs, *Arctic and Alpine Research*, 29, 3, 345-351.

1024 Eicken, H. W.B. Tucker III and D.K. Perovich (2001), Indirect measurements of the mass balance of
1025 summer Arctic sea ice with an electromagnetic induction technique, *Ann. Glaciol. 33*, 194–200.

1026 Eicken, H., H. R. Krouse, D. Kadko, and D. K. Perovich (2002), Tracer studies of pathways and rates of
1027 meltwater transport through Arctic summer sea ice, *J. Geophys. Res.*, *107*(C10), 8046,
1028 doi:10.1029/2000JC000583.

1029 Eicken, H., T. C. Grenfell, D. K. Perovich, J. A. Richter-Menge, and K. Frey (2004), Hydraulic controls of
1030 summer Arctic pack ice albedo*, J. Geophys. Res.*, 109, C08007, doi:10.1029/2003JC001989.

1031 Fetterer, F., and N. Untersteiner (1998), Observations of melt ponds on Arctic sea ice, *J. Geophys.*
1032 *Res.*, *103*(C11), 24,821–24,835, doi:10.1029/98JC02034.

1033 Flocco, D., and D. L. Feltham (2007), A continuum model of melt pond evolution on Arctic sea ice*, J.*
1034 *Geophys. Res., 112*, C08016, doi:10.1029/2006JC003836.

1035 Flocco, D., D. L. Feltham, and A. K. Turner (2010), Incorporation of a physically based melt pond scheme
1036 into the sea ice component of a climate model, *J. Geophys. Res.*, *115*, C08012,
1037 doi:10.1029/2009JC005568.

1038 Frankenstein, G. and R. Garner (1967), Equations for determining the brine volume of sea ice from -0.5^{o} to
1039 -22.9^{o}C, *Journal of Glaciology*, *6*, 48, 943-44.

1040 Freitag, J., and Eicken, H. (2003), Meltwater circulation and permeability of Arctic summer sea ice derived
1041 from hydrological field experiments, *J. of Glaciology*, *49*, 349-358.

1042 Golden, K.M. (2001), Brine percolation and the transport properties of sea ice, *Ann. Glaciol. 33*, pp. 28–36.

1043 Golden, K.M., S.F. Ackley, and V.I. Lytle (1998), The percolation phase transition in sea ice, *Science, 282,*
1044 2238–2241.

1045 Golden, K. M., H. Eicken, A. L. Heaton, J. Miner, D. J. Pringle, and J. Zhu (2007), Thermal evolution of
1046 permeability and microstructure in sea ice, *Geophys. Res. Lett.*, *34*, L16501,
1047 doi:10.1029/2007GL030447.
1048 Granskog, M.A., T. Vihma, R. Pirazzini and B. Cheng (2006), Superimposed ice formation and surface
1049 energy fluxes on sea ice during the spring melt–freeze period in the Baltic Sea, *J. Glaciol.,*
1050 *52*(176), 119–127.
1051 Grenfell, T. C., and D. K. Perovich (2004), Seasonal and spatial evolution of albedo in a snow-ice-land-
1052 ocean environment, *J. Geophys. Res.*, *109*, C01001, doi:10.1029/2003JC001866.
1053 Holt, B., and S. A. Digby (1985), Processes and Imagery of First-Year Fast Sea Ice During the Melt
1054 Season, *J. Geophys. Res.*, *90*(C3), 5045–5062, doi:10.1029/JC090iC03p05045.
1055 Hunke, E. C. and W. H. Lipscomb (2010), CICE: the Los Alamos Sea Ice Model Documentation and
1056 Software User's Manual Version 4.1 LA-CC-06-012, *T-3 Fluid Dynamics Group, Los Alamos*
1057 *National Laboratory*.
1058 Kawamura, T., M. Ishikawa, T. Takatsuka, S. Kojima, and K. Shirasawa (2006), Measurements of
1059 Permeability in Sea Ice, *Proceedings of the 18th IAHR Intern. Symposium on Sea Ice*, 105-112.
1060 Kelly, B.P. (1996), Live Capture of Ringed Seals in Ice-Covered Waters. *The Journal of Wildlife*
1061 *Management, 60*, 3, 678-684.
1062 Lake, R. A., and E.L. Lewis (1970), Salt rejection by sea ice during growth, *J. Geophys. Res. 75* (3), 583–
1063 597.
1064 Light, B., T. C. Grenfell, and D. K. Perovich (2008), Transmission and absorption of solar radiation by
1065 Arctic sea ice during the melt season, *J. Geophys. Res., 113*, C03023, doi:10.1029/2006JC003977.
1066 Lüthje, M., D. L. Feltham, P. D. Taylor, and M. G. Worster (2006), Modeling the summertime evolution of
1067 sea-ice melt ponds, *J. Geophys. Res.*, *111*, C02001, doi:10.1029/2004JC002818.
1068 Ono, N., and T. Kasai (1985), Surface layer salinity of young sea ice, *Ann. Glaciol.*, *6*, 298–299.
1069 Pedersen, C. A., E. Roeckner, M. Lüthje, and J. Winther (2009), A new sea ice albedo scheme including
1070 melt ponds for ECHAM5 general circulation model, *J. Geophys. Res.*, *114*, D08101,
1071 doi:10.1029/2008JD010440.
1072 Perovich, D. K., and A. J. Gow (1996), A quantitative description of sea ice inclusions, *J. Geophys.*

Res., *101*(C8), 18,327–18,343, doi:10.1029/96JC01688.

Perovich, D. K., T. C. Grenfell, B. Light, and P. V. Hobbs (2002a), Seasonal evolution of the albedo of multiyear Arctic sea ice, *J. Geophys. Res., 107* (C10), 8044, doi:10.1029/2000JC000438.

Perovich, D. K., W. B. Tucker III, and K. A. Ligett (2002b), Aerial observations of the evolution of ice surface conditions during summer, *J. Geophys. Res.*, *107* (C10), 8048, doi:10.1029/2000JC000449.

Perovich, D. K., T. C. Grenfell, J. A. Richter-Menge, B. Light, W. B. Tucker III, and H. Eicken (2003), Thin and thinner: Sea ice mass balance measurements during SHEBA, *J. Geophys. Res., 108* (C3), 8050, doi:10.1029/2001JC001079.

Petrich, C., P. J. Langhorne, and Z. F. Sun (2006), Modelling the interrelationships between permeability, effective porosity, and total porosity in sea ice, *Cold Reg. Sci. Technol*., 44, 131 – 144.

Pringle, D. J., J. E. Miner, H. Eicken, and K. M. Golden (2009), Pore space percolation in sea ice single crystals, *J. Geophys. Res.*, *114*, C12017, doi:10.1029/2008JC005145.

Rantz, S. E. and others (2005), Measurement and Computation of Streamflow, *US Geological Survey,* Water Supply Paper 2175.

Scharien, R. K. and J. J. Yackel (2005), Analysis of surface roughness and morphology of first-year sea ice melt ponds: Implications for microwave scattering*, IEEE Trans. Geosci. Remote Sens*. *43*, 2927 2005.

Shapiro, L. H., and P. W. Barnes (1991), Correlation of nearshore ice movement with seabed ice gouges near Barrow, Alaska, *J. Geophys. Res., 96*(C9), 16,979 – 16,989.

Skyllingstad, E. D., C. A. Paulson, and D. K. Perovich (2009), Simulation of melt pond evolution on level ice, *J. Geophys. Res.*, *114*, C12019, doi:10.1029/2009JC005363.

Taylor, P. D., and D. L. Feltham (2004), A model of melt pond evolution on sea ice, *J. Geophys. Res., 109*, C12007, doi:10.1029/2004JC002361.

Tschundi, M., J. Maslanik, and D. Perovich (2008), Derivation of melt pond coverage on Arctic sea ice using Modis observations. *Remote Sensing of Environment. 112*, 2605-2614.

Figure Captions

Figure 1 – A compilation of published pond coverage data plotted on a time scale normalized to the start of pond formation. Solid markers denote FYI measurements while hollow markers denote multiyear or mixed ice measurements.

Figure 2 – Idealized illustration of a melt pond, showing meltwater flux pathways.

Figure 3 – Schematic of a typical observation site.

Figure 4 – Aerial view of the 2009 north site drainage basin taken 8 June with drainage flaws on 10 June marked.

Figure 5 – (a) melt pond coverage vs. calendar date, (b) melt pond coverage vs. days since onset of pond formation, (c) spatially averaged surface albedo vs. days since onset of pond formation, (d) spatially averaged surface albedo vs. melt pond coverage.

Figure 6 – Composite of kite and plane based aerial photos and height colored surface maps created from TLS during melt season at the 2009 north site. There is a scale on the lower right aerial photo while the TLS images are 100 m x 200 m in size. All images are dated in the upper left corner.

Figure 7 – Comparison of observed pond coverage and GCM pond parameterizations.

Figure 8 – (a) Melt pond fraction vs. average pond depth observed during 2009 (b) Total meltwater generation vs. meltwater retained at the ice surface for the 2009 sites.

Figure 9 – (a) Cumulative distribution of pre-melt surface height at pond covered locations by date at 2009 south site and (b) Pond coverage fraction as a function of pre-melt surface height at 2009 south site.

Figure 10 – Height colored pre-melt surface map of (a) entire 2009 north site on 28 May and (b) the areas which are pond covered on 7 June.

Figure 11 – Ice surface on 13 June 2009 at the north site with (a) all areas where ponds form between 13 June and 23 June highlighted in blue, and (b) all areas within 7cm of sea level on 13 June. There is a very strong spatial correlation between pond growth and low surface elevation.

Figure 12 – Cumulative surface height distribution at 2009 north site of entire surface on 13 June and of just those areas where ponds grow between 13 June and 23 June.

Figure 13 – Cumulative surface height distributions between 13 June and 23 June showing little changed availability of surfaces within 5 cm of sea level available for flooding by an incremental drop in freeboard.

Figure 14 – Total meltwater lost from the surface of the ice and meltwater measured flowing down macroscopic holes are plotted with pond coverage. Markers i, ii, and iii denote the start of pond formation, the date macroscopic flaws appear, and the date ponds reach sea level.

Figure 15 – Composite of photos showing the evolution of brine channels to macroscopic drainage holes.

Figure 16 – (a) Profiles of salinity and (b) calculated porosity from ice cores in late winter and early spring. Freshening in the upper ice (dashed oval) during May corresponds temporally to increases in porosity above 5%. Data from the Barrow Ice Observatory http://seaice.alaska.edu/gi/observatories. (c) Profiles of salinity and (d) temperature in ice cores taken later in the melt season beneath ponds. Note gradual freshening up upper ice layers until the onset of percolation about13 June, when salinity begins to drop throughout the ice column, indicating flushing.

Figure 17 – Image of highly porous melting superimposed ice breaking away from pond bottoms on 7 June 2009.

Figure 18 – Percentage of all ponds along transects lined with superimposed ice vs. date. Superimposed ice is removed several days prior to the onset of percolation on 13 Jun.

Figure 19 – Aerial photos of a small basin taken on 10 June (a) and 13 June (b). LiDAR observations on the morning of 11 June showed that drainage had barely begun and the scene looked very similar to 10 June, while by the evening the scene looked essentially as it did on 13 June when the second picture was taken.

Figure 20 – Profiles of $\delta\,^{2}H$ and $\delta\,^{18}O$ stable isotopes taken in 2010 from cores beneath melt ponds.

Figure 21 – Minimum diameter of modeled flow channels vs. time for varying starting diameters in 5 June 2009 ice temperature and salinity conditions.

Figure 22 – Critical pore diameter vs. date for three desalination schemes

Tables:

Table 1: Shortwave Fluxes and Potential Impact of Albedo Varations

	Average	Daily StDev	Daily Min	Daily Max
2008-2010 Solar Insolation (W/m^{-2})	254	57	135	369
Net Shortwave, Albedo = 0.25	191	43	101	277
Net Shortwave, Albedo = 0.60	102	23	54	148
Difference	89	20	47	129
Enough to melt cm of ice /day	2.3	0.5	1.2	3.3

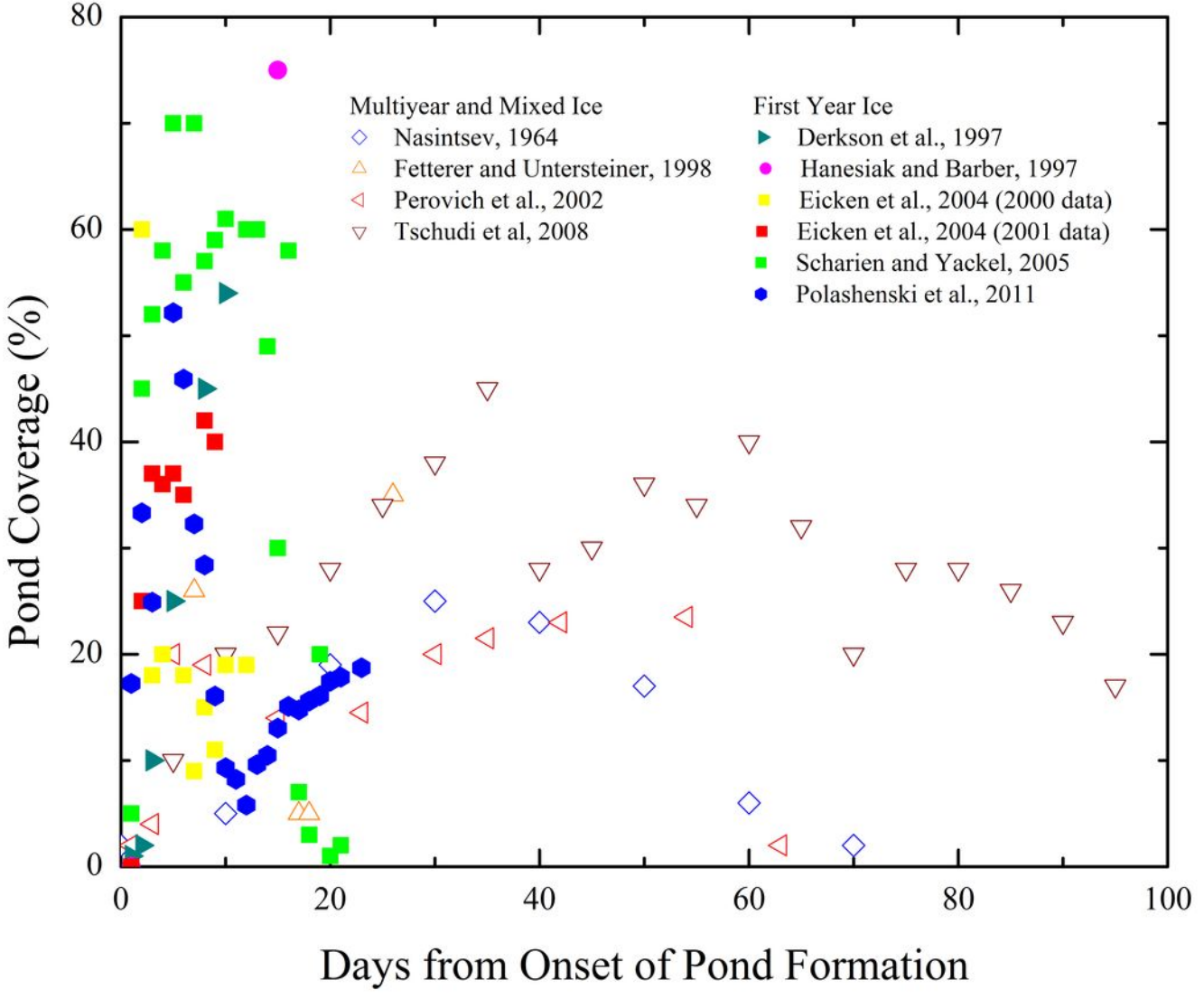
Multiyear and Mixed Ice
Nasintsev, 1964
Fetterer and Untersteiner, 1998
Perovich et al., 2002
Tschudi et al, 2008
First Year Ice
Derkson et al., 1997
Hanesiak and Barber, 1997
Eicken et al., 2004 (2000 data)
Eicken et al., 2004 (2001 data)
Scharien and Yackel, 2005
Polashenski et al., 2011
Pond Coverage (%)
Days from Onset of Pond Formation
0
20
40
60
80
100

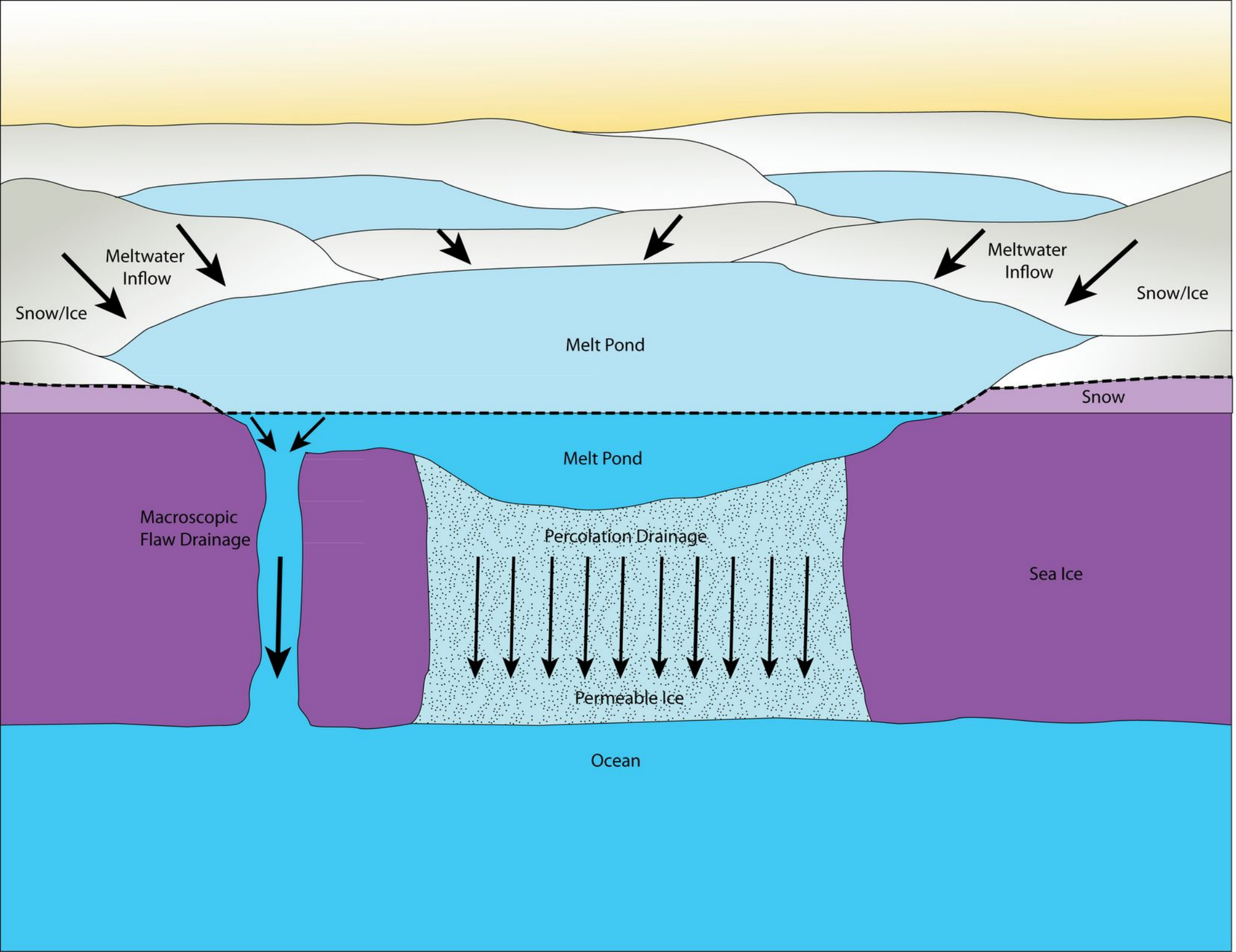
Meltwater
Inflow
Snow/Ice
Meltwater
Inflow
Snow/Ice
Melt Pond
Snow
Melt Pond
Macroscopic
Flaw Drainage
Percolation Drainage
Sea Ice
Permeable Ice
Ocean

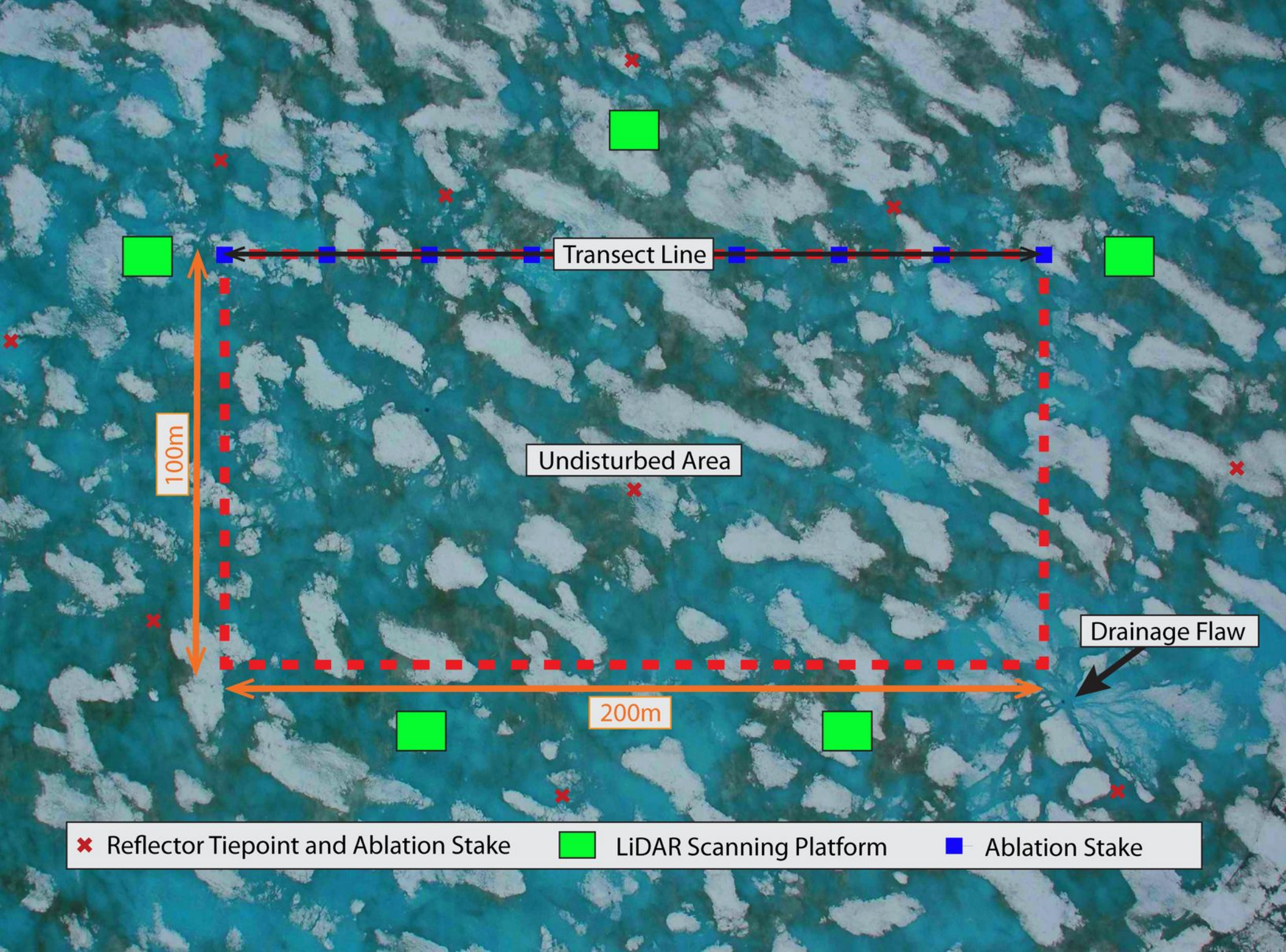
Transect Line
100m
Undisturbed Area
Drainage Flaw
200m
Reflector Tiepoint and Ablation Stake
LiDAR Scanning Platform
Ablation Stake

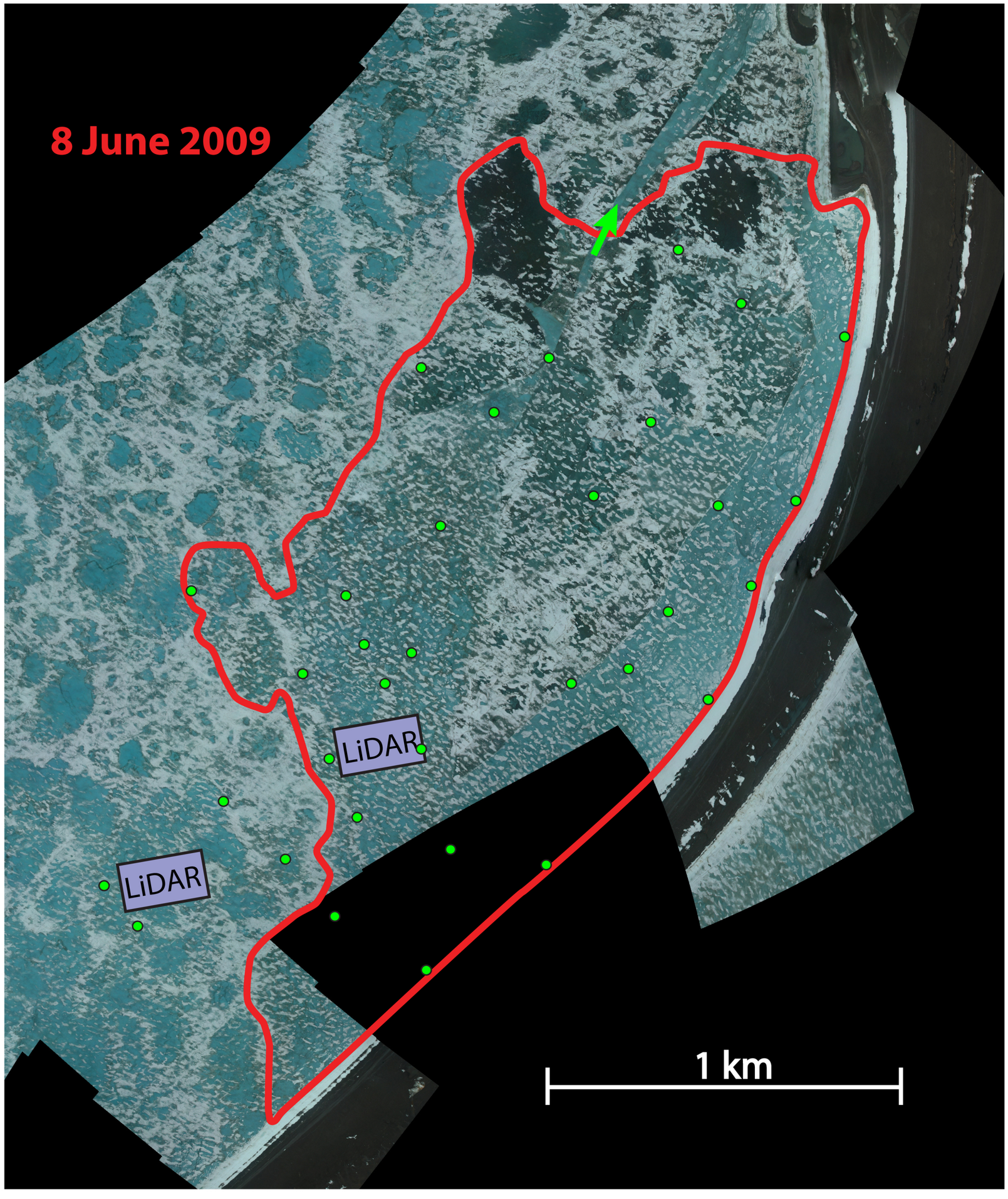
8 June 2009
LiDAR
LiDAR
1 km

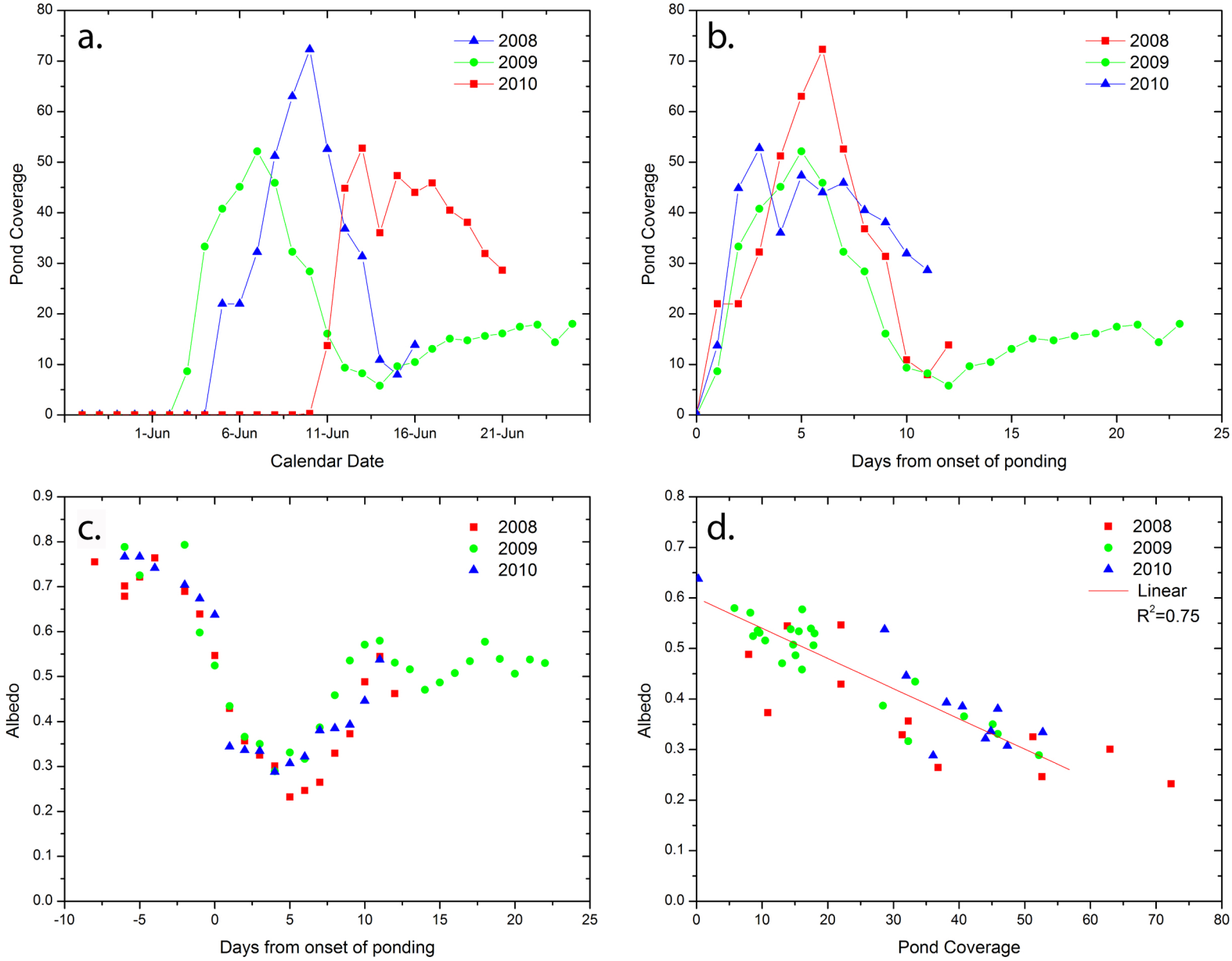
a.
2008
2009
2010
Pond Coverage
Calendar Date
1-Jun
6-Jun
11-Jun
16-Jun
21-Jun
b.
Days from onset of ponding
c.
Albedo
d.
Linear
R2=0.75
Pond Coverage

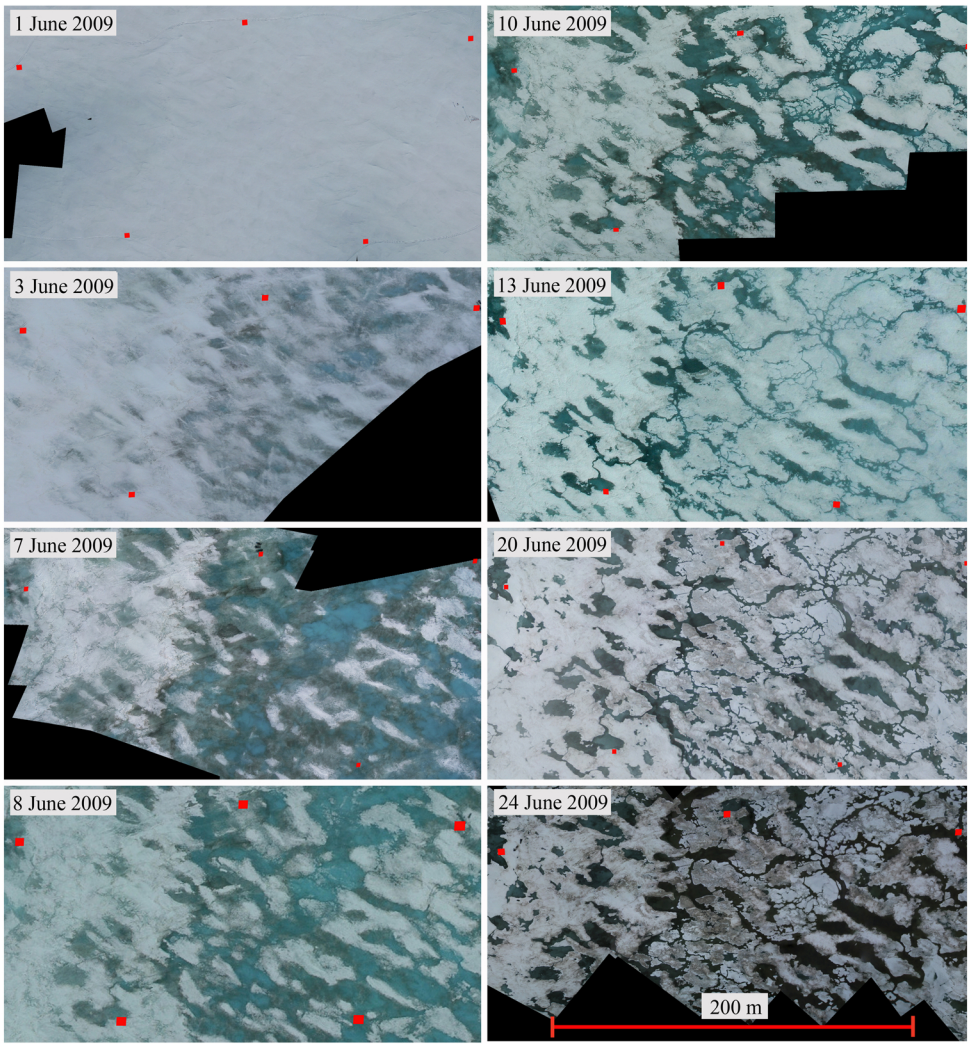

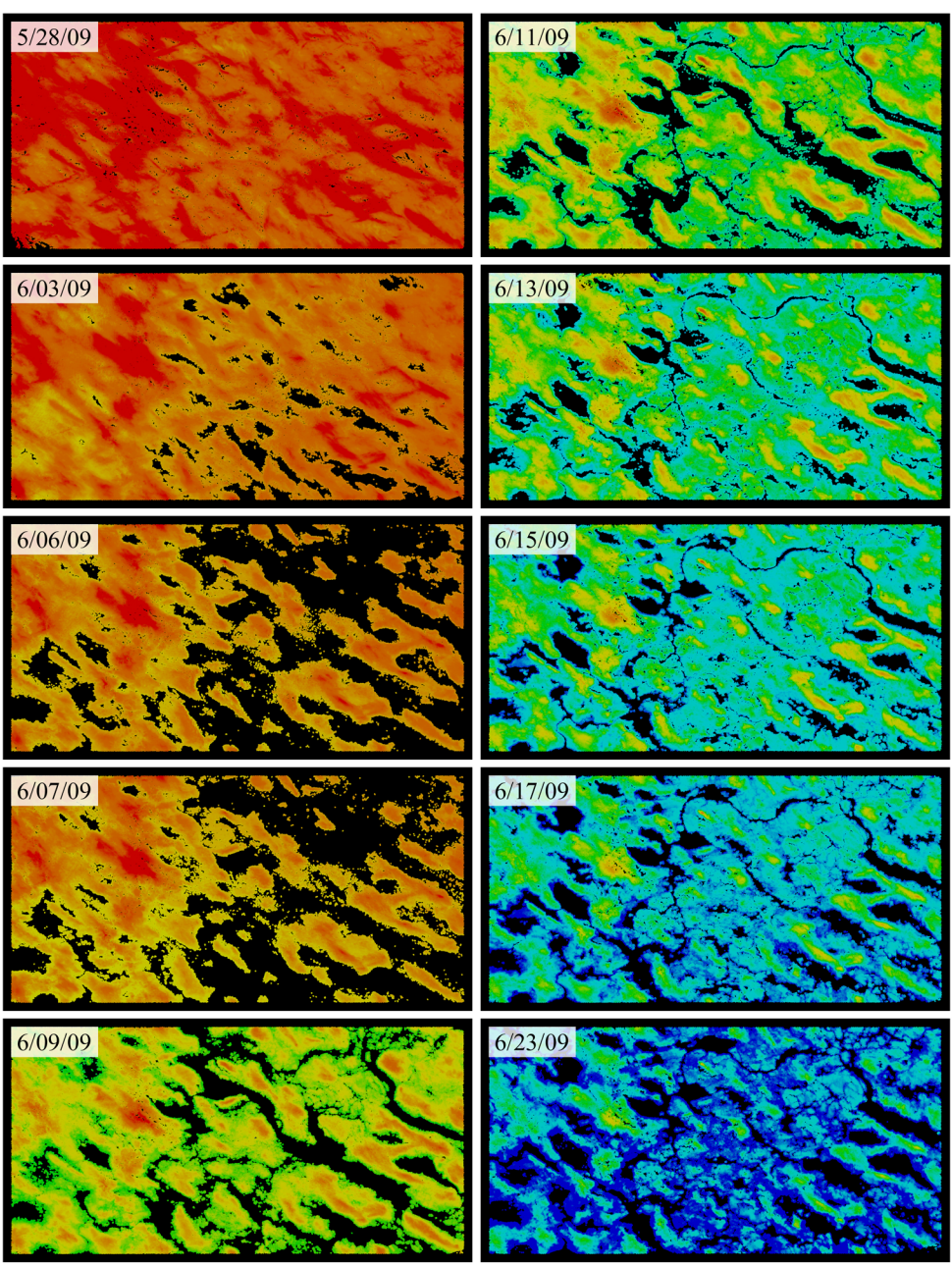

Surface Heights

2009 North Site

0m 0.6m

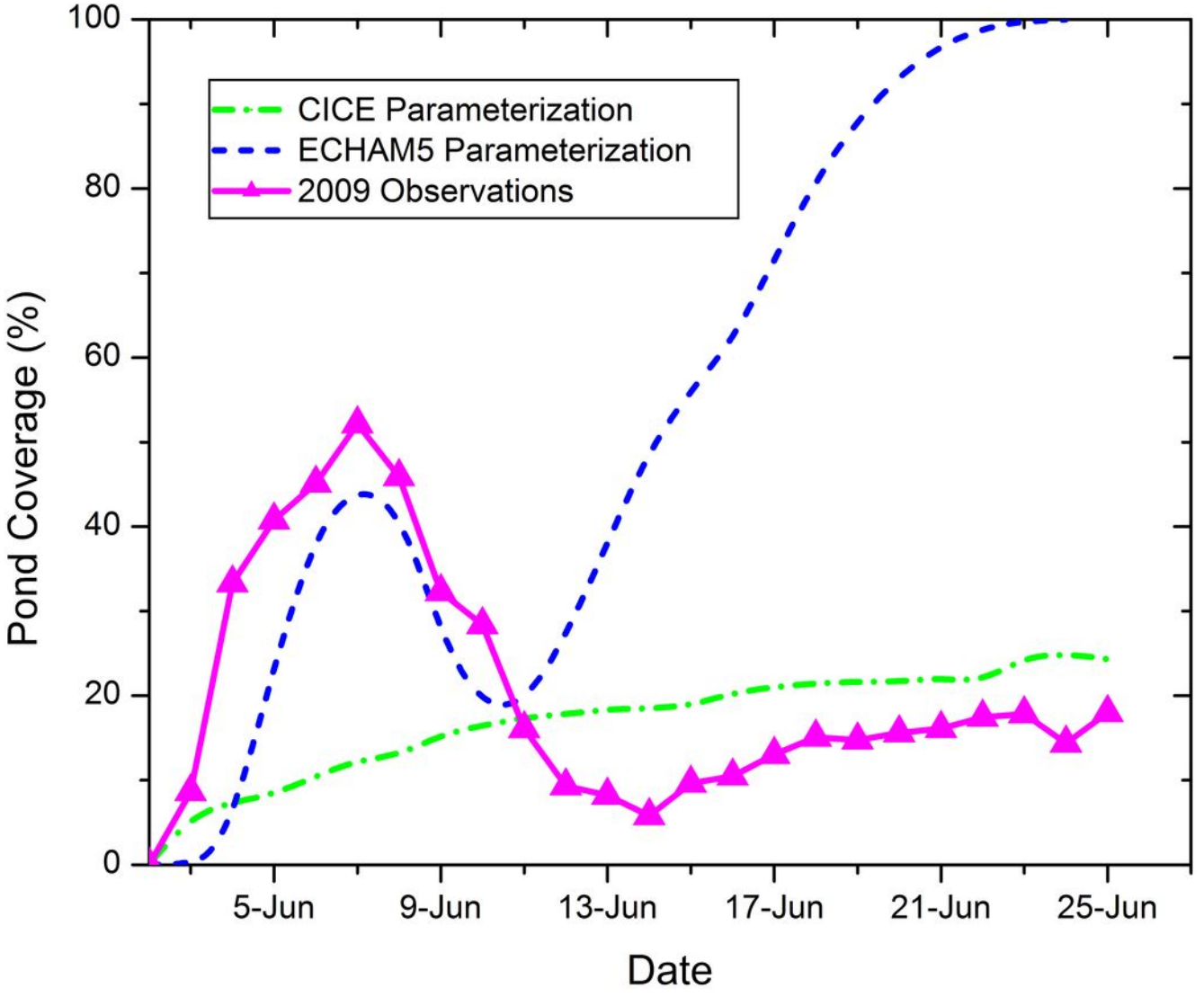
CICE Parameterization
ECHAM5 Parameterization
2009 Observations
Pond Coverage (%)
0
20
40
60
80
100
5-Jun
9-Jun
13-Jun
17-Jun
21-Jun
25-Jun
Date

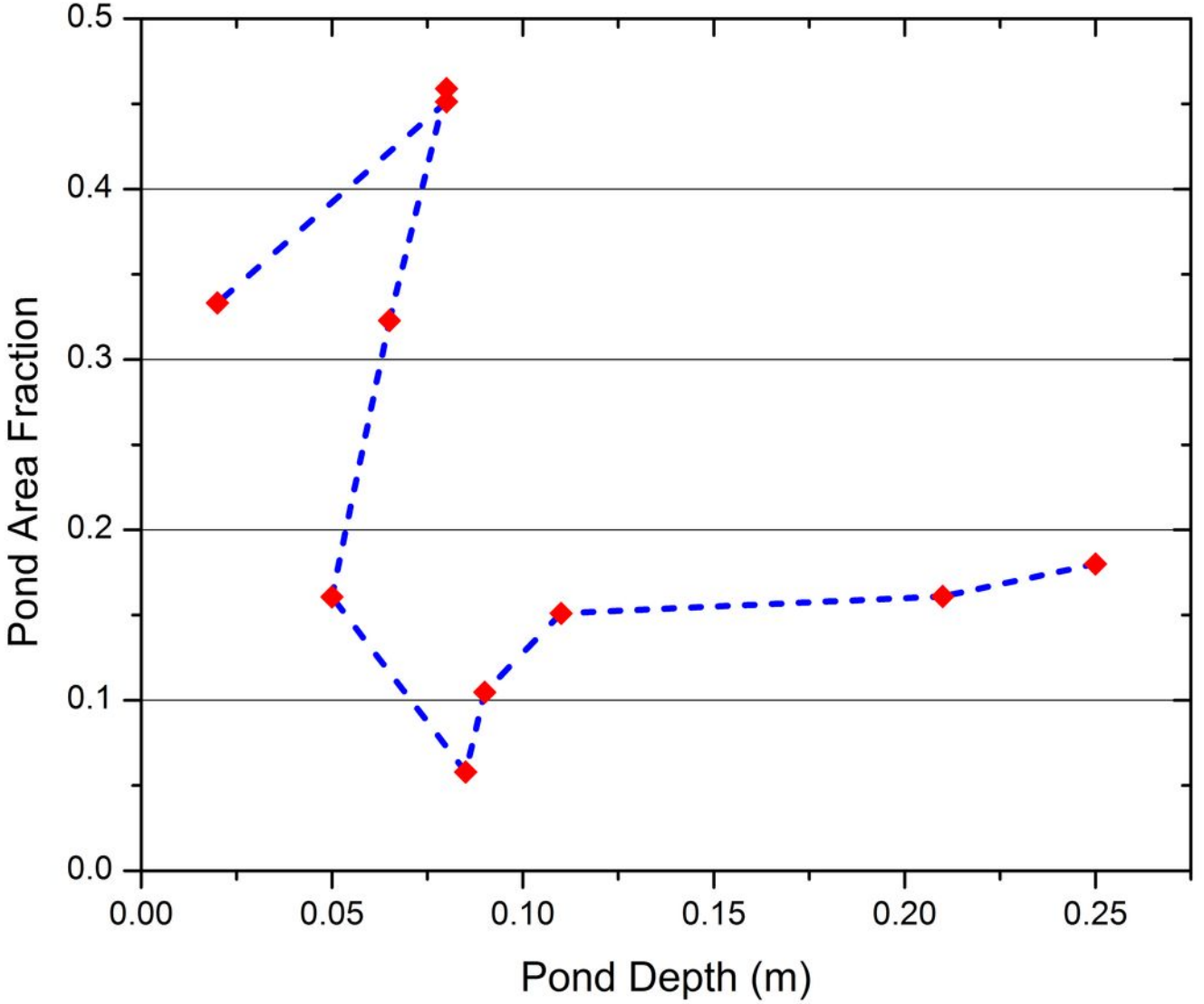
0.5
0.4
0.3
0.2
0.1
0.0
Pond Area Fraction
0.00
0.05
0.10
0.15
0.20
0.25
Pond Depth (m)

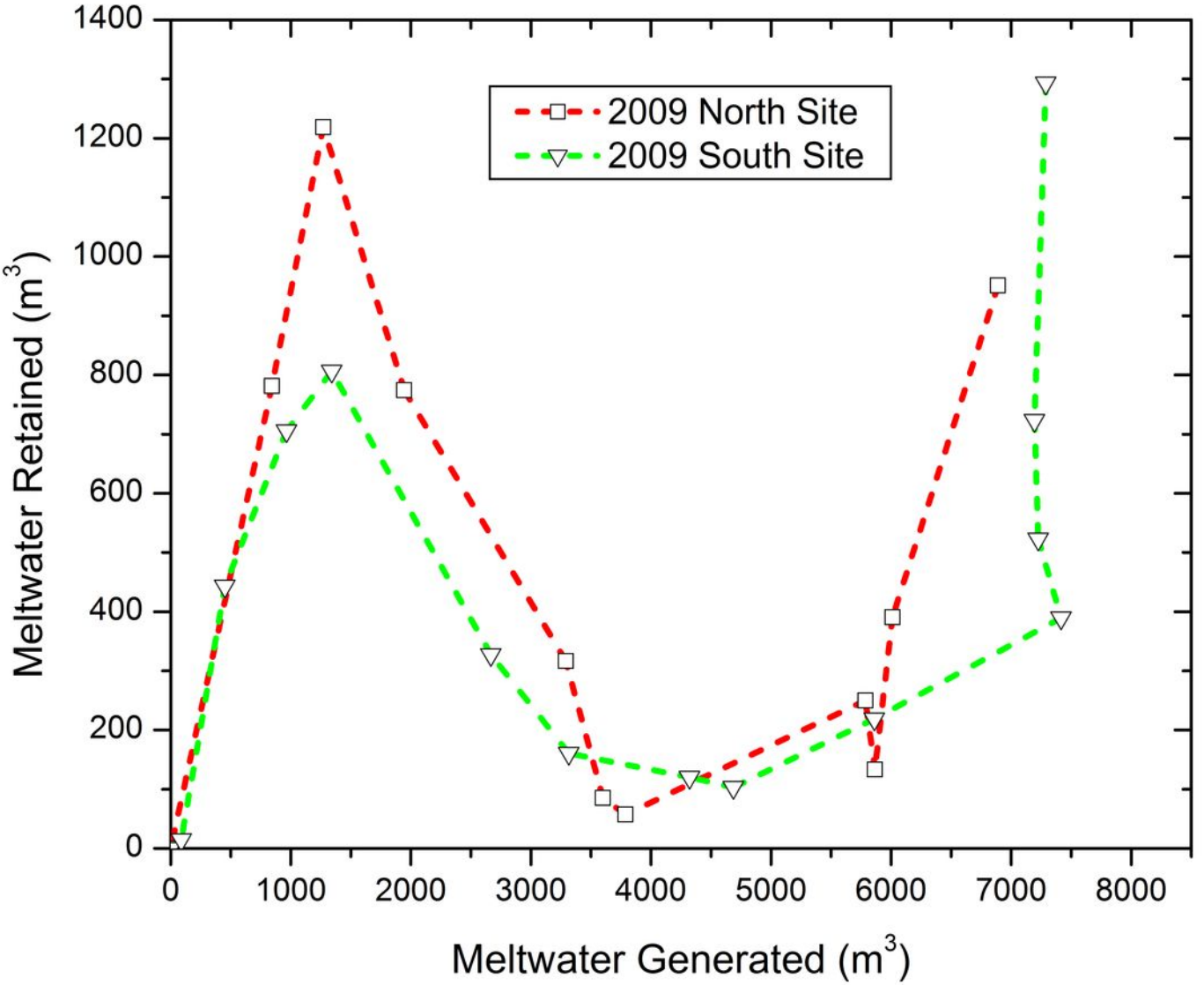
2009 North Site
2009 South Site
Meltwater Retained (m3)
Meltwater Generated (m3)
0
200
400
600
800
1000
1200
1400
0
1000
2000
3000
4000
5000
6000
7000
8000

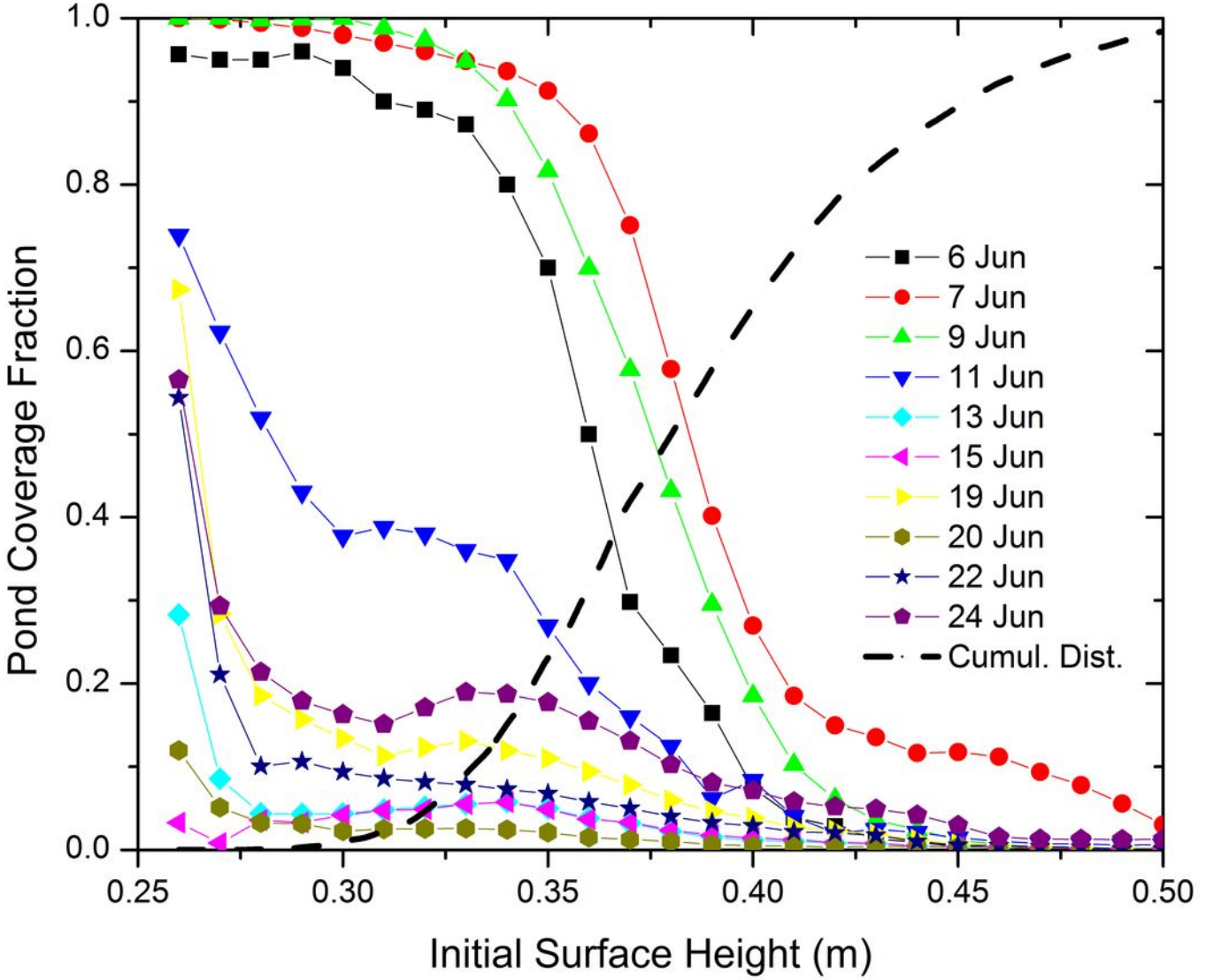
Pond Coverage Fraction
Initial Surface Height (m)
1.0
0.8
0.6
0.4
0.2
0.0
0.25
0.30
0.35
0.40
0.45
0.50
6 Jun
7 Jun
9 Jun
11 Jun
13 Jun
15 Jun
19 Jun
20 Jun
22 Jun
24 Jun
Cumul. Dist.

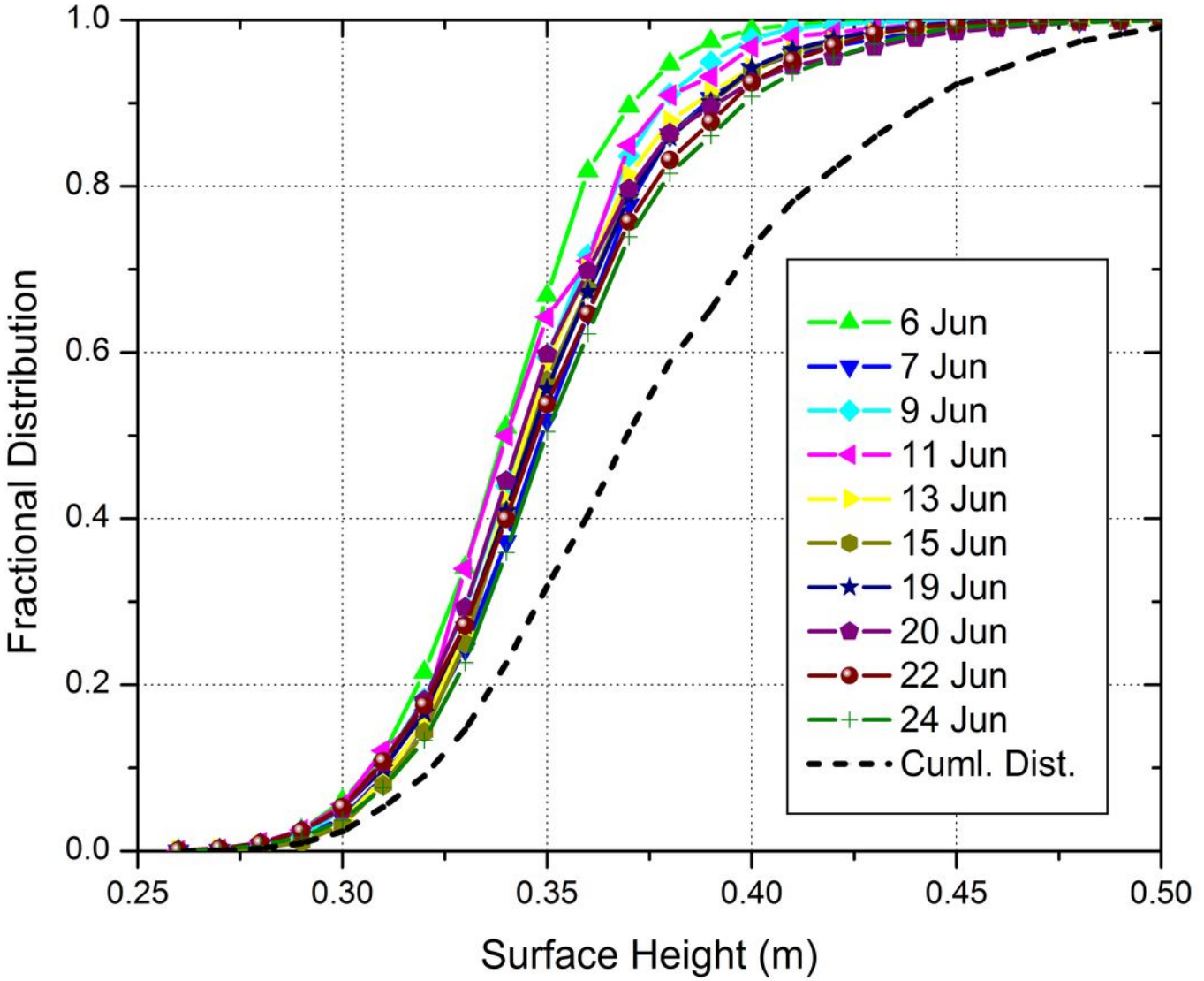
Fractional Distribution
Surface Height (m)
1.0
0.8
0.6
0.4
0.2
0.0
0.25
0.30
0.35
0.40
0.45
0.50
6 Jun
7 Jun
9 Jun
11 Jun
13 Jun
15 Jun
19 Jun
20 Jun
22 Jun
24 Jun
Cuml. Dist.

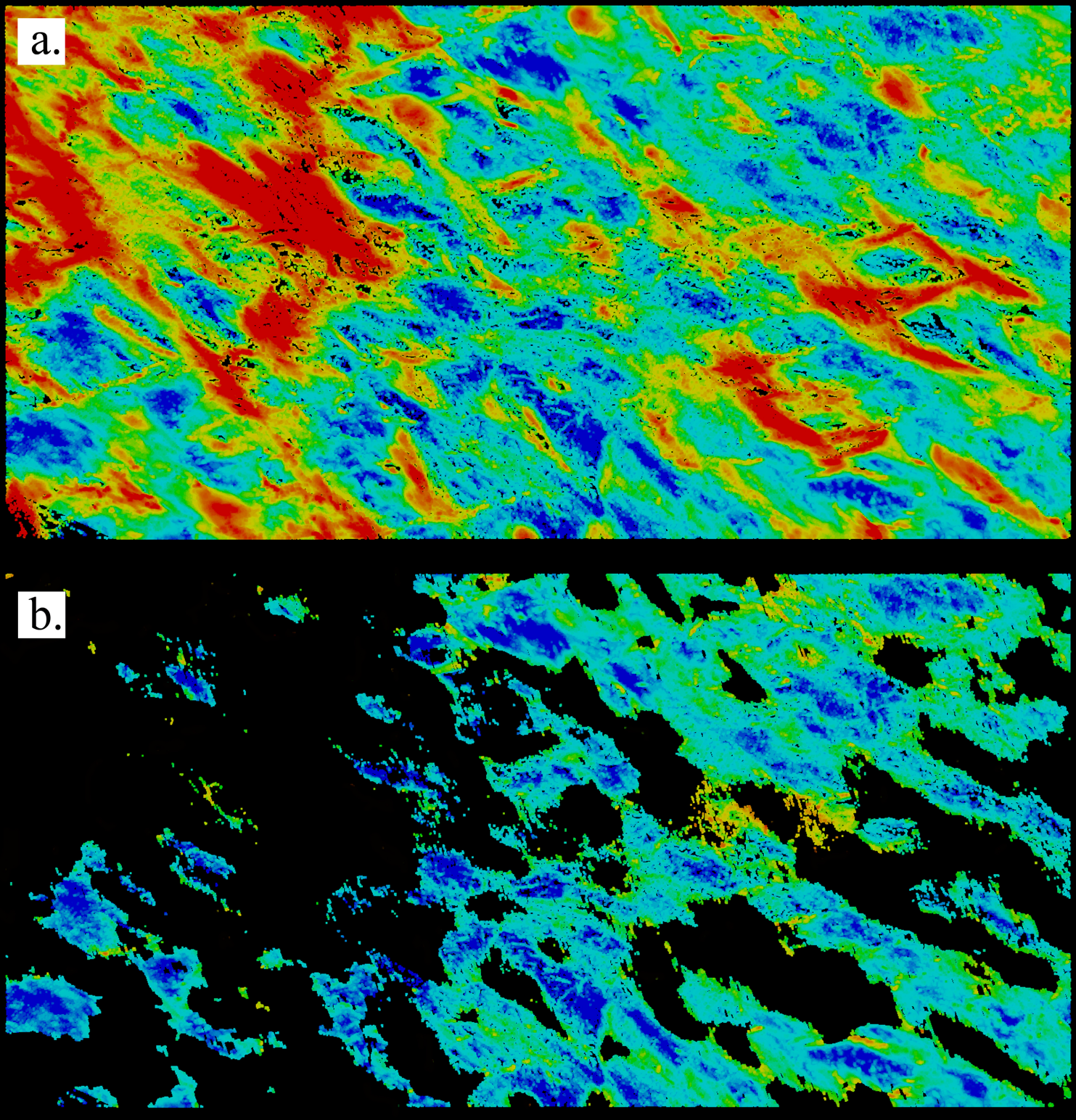
a.
b.

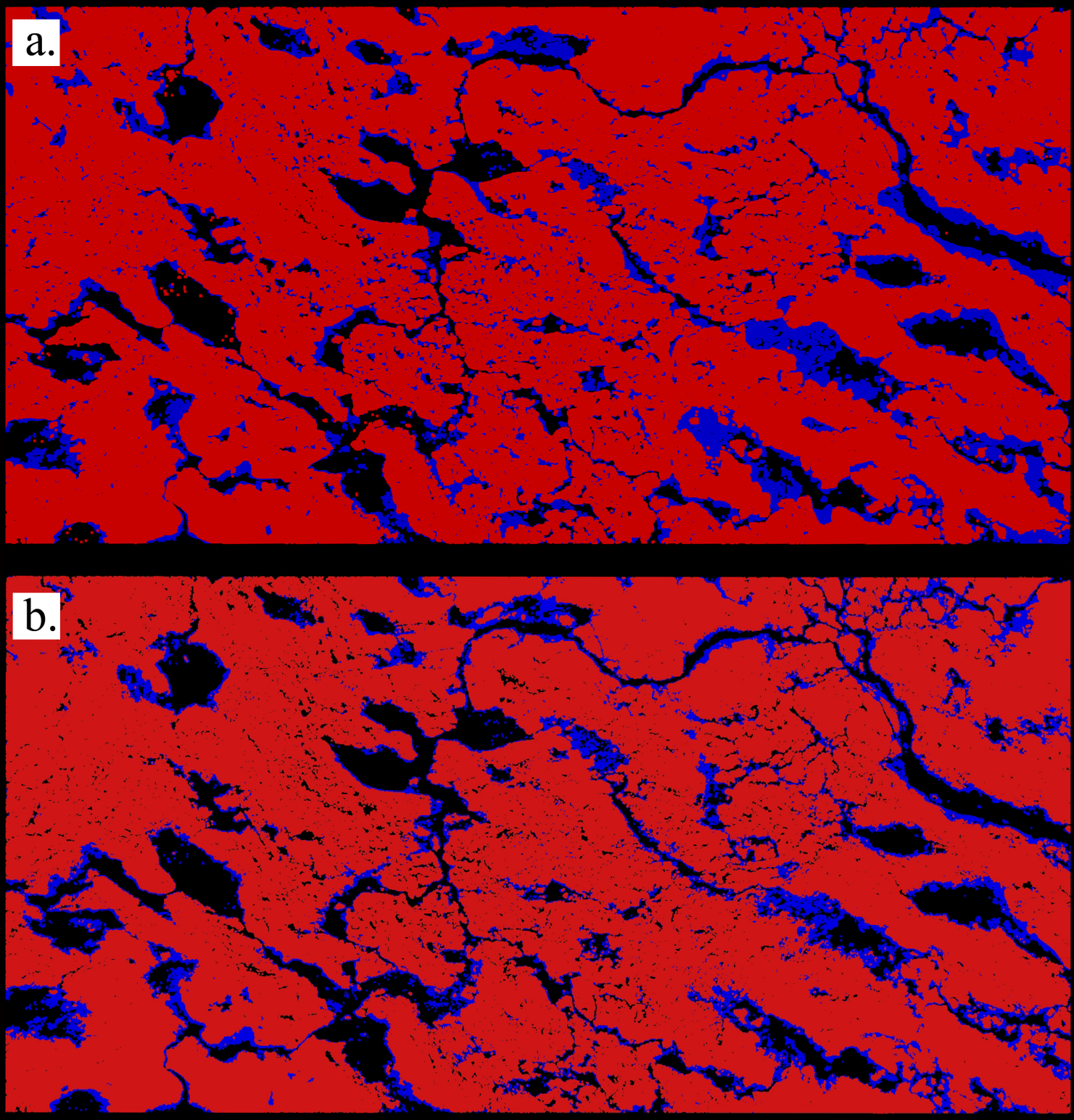
a.
b.

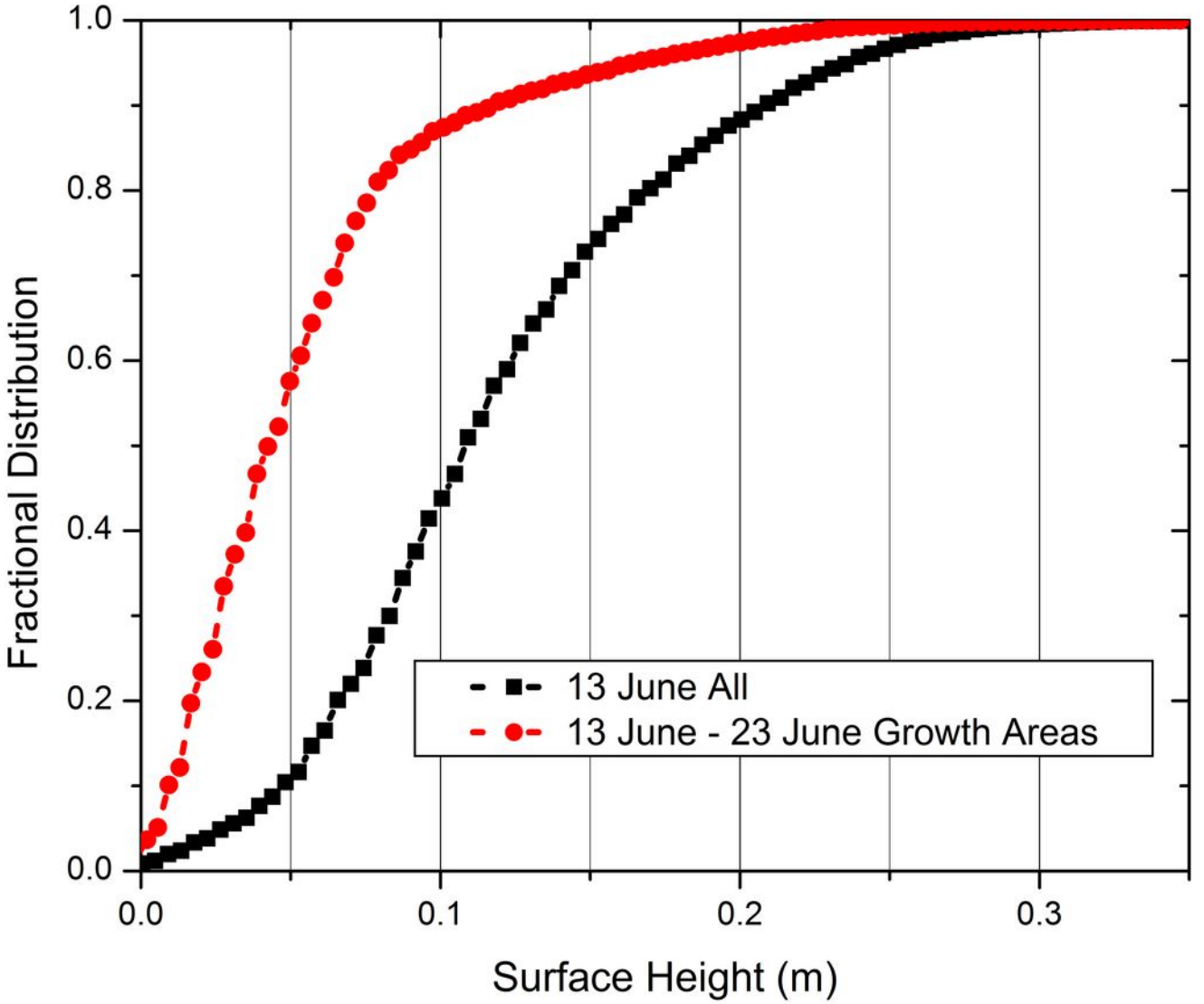
1.0
0.8
0.6
0.4
0.2
0.0
Fractional Distribution
0.0
0.1
0.2
0.3
Surface Height (m)
13 June All
13 June - 23 June Growth Areas

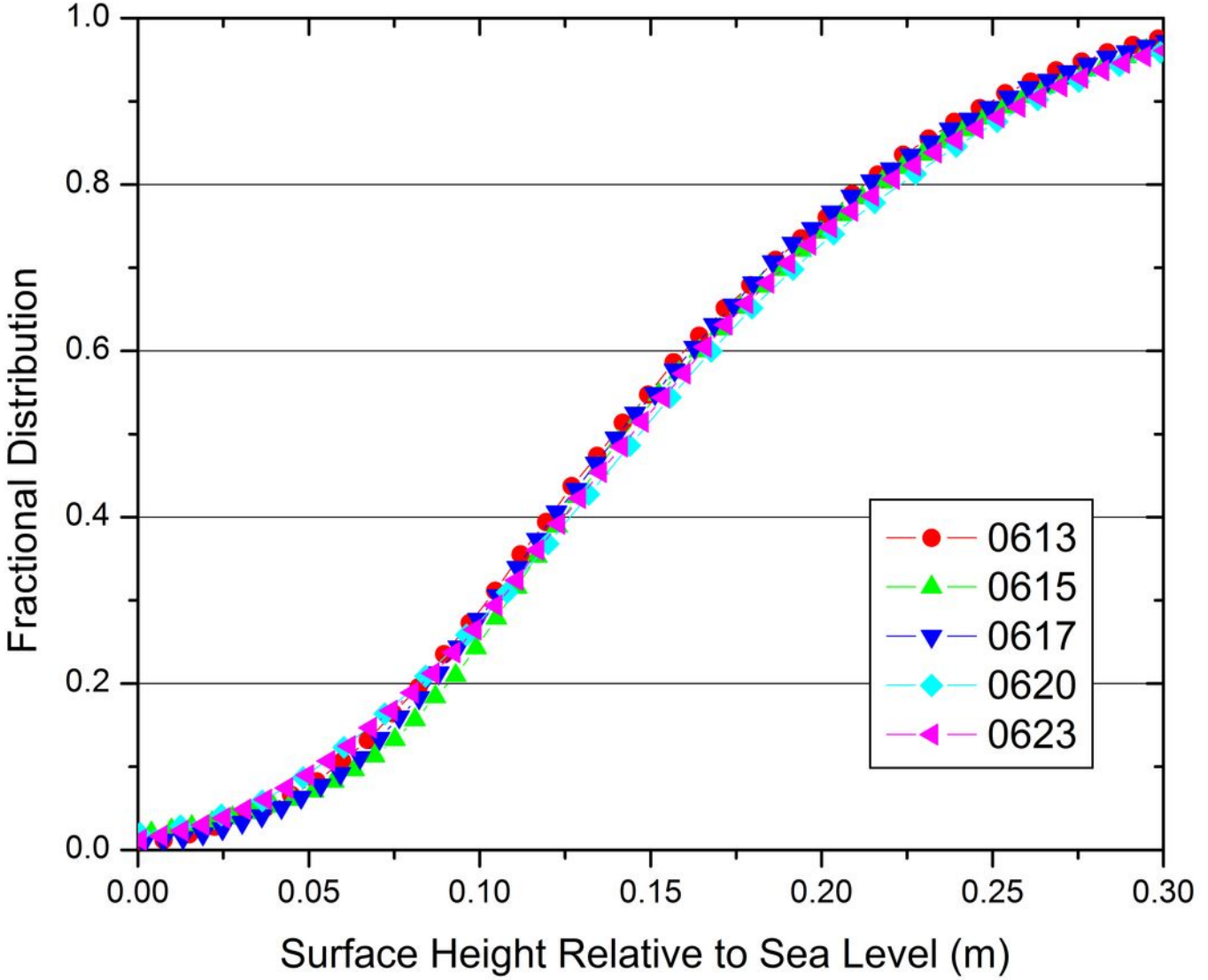
1.0
0.8
0.6
0.4
0.2
0.0
Fractional Distribution
0.00
0.05
0.10
0.15
0.20
0.25
0.30
Surface Height Relative to Sea Level (m)
0613
0615
0617
0620
0623

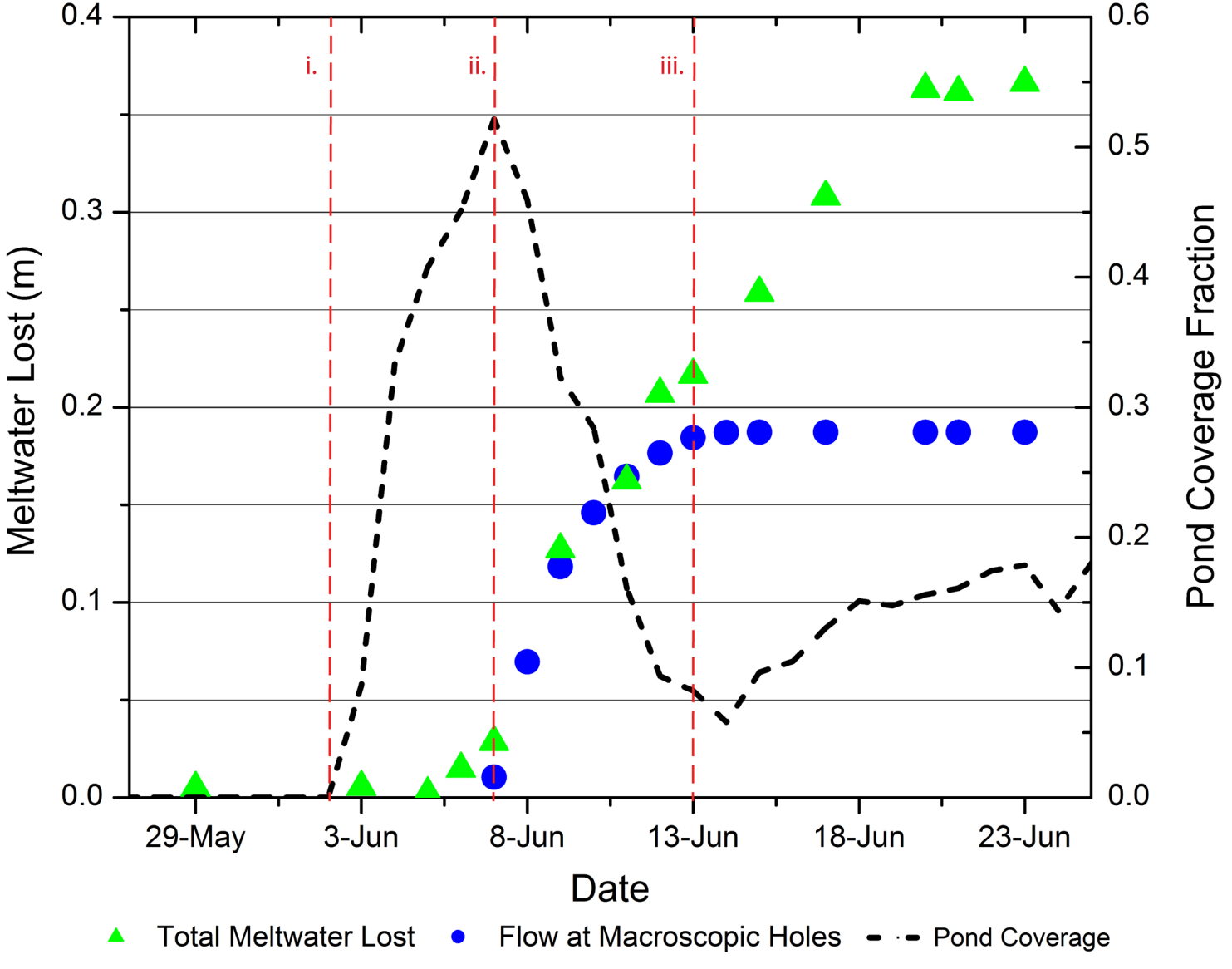
0.4
0.3
0.2
0.1
0.0
Meltwater Lost (m)
0.6
0.5
0.4
0.3
0.2
0.1
0.0
Pond Coverage Fraction
i.
ii.
iii.
29-May
3-Jun
8-Jun
13-Jun
18-Jun
23-Jun
Date
Total Meltwater Lost
Flow at Macroscopic Holes
Pond Coverage

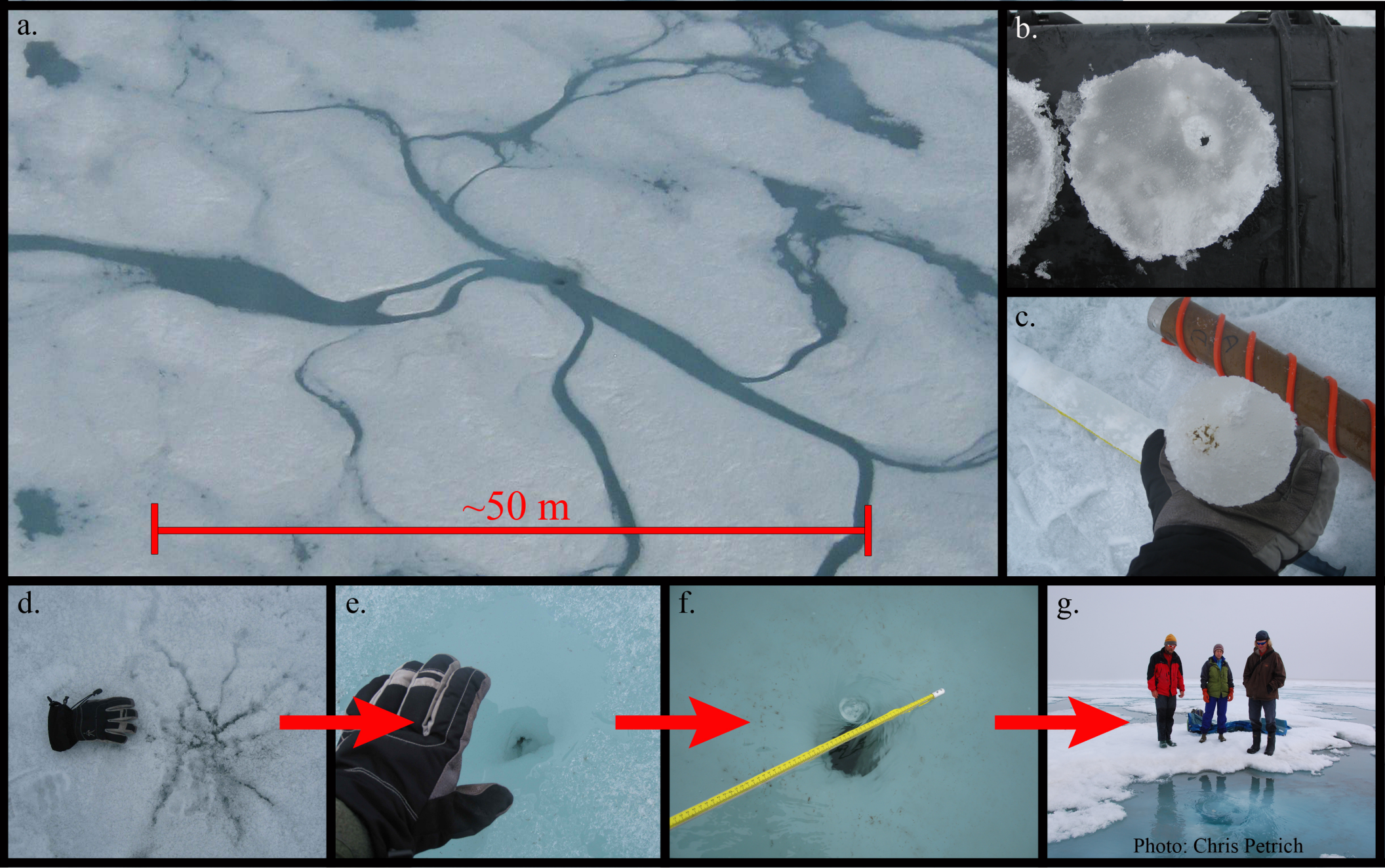
a.
~50 m
b.
c.
d.
e.
f.
g.
Photo: Chris Petrich

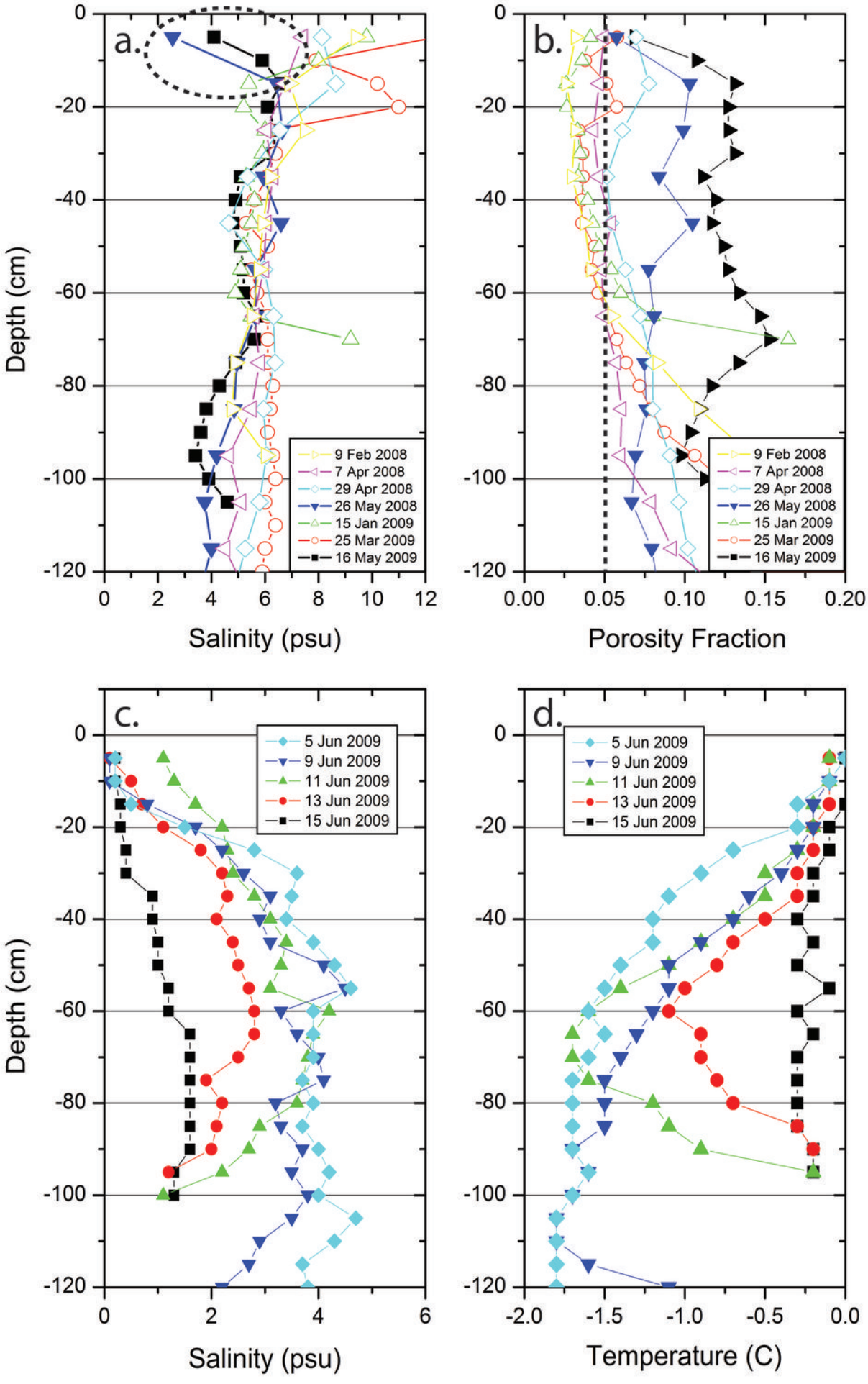
a.
b.
c.
d.
Depth (cm)
Salinity (psu)
Porosity Fraction
Temperature (C)
9 Feb 2008
7 Apr 2008
29 Apr 2008
26 May 2008
15 Jan 2009
25 Mar 2009
16 May 2009
5 Jun 2009
9 Jun 2009
11 Jun 2009
13 Jun 2009
15 Jun 2009

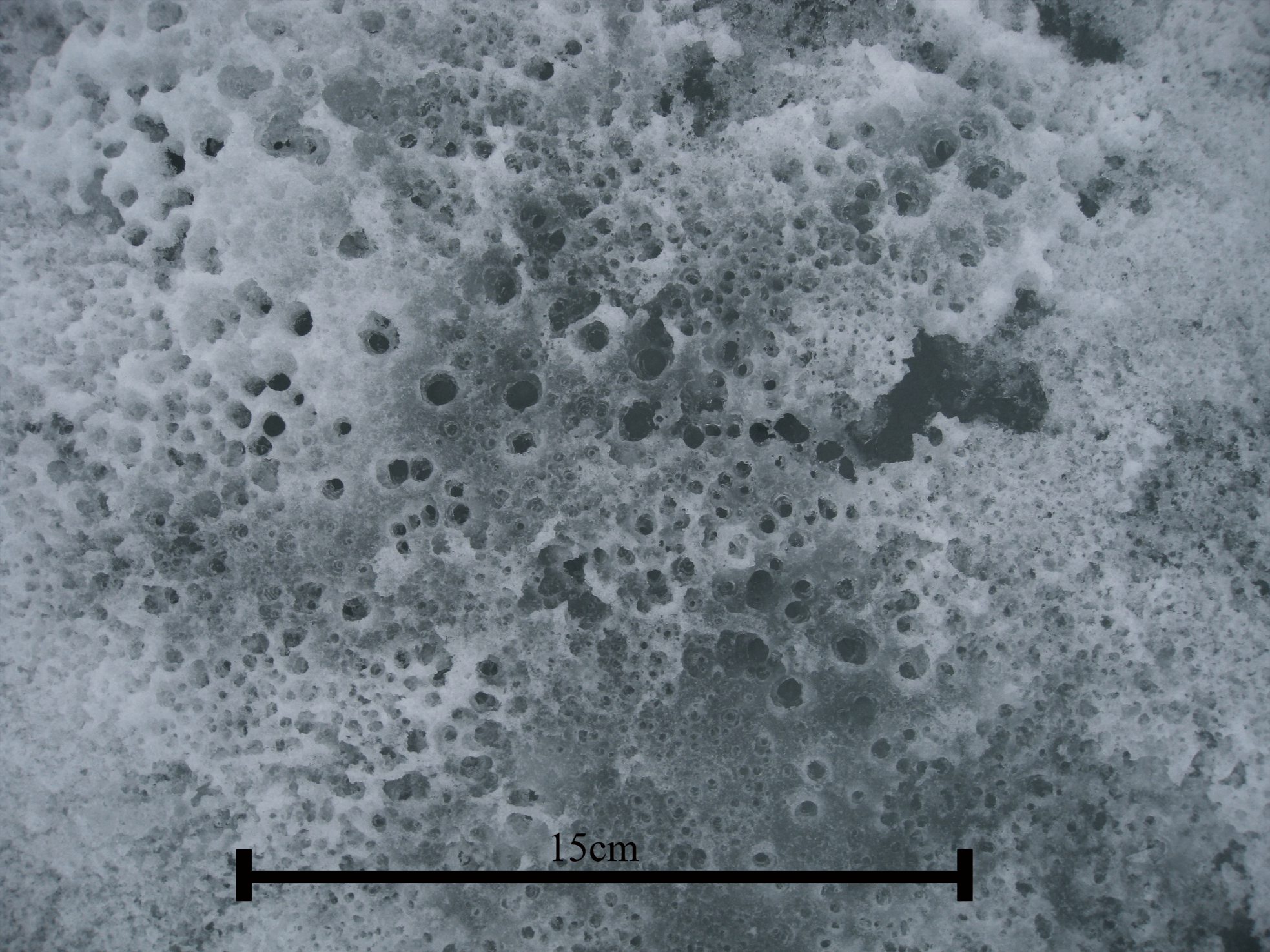
15cm

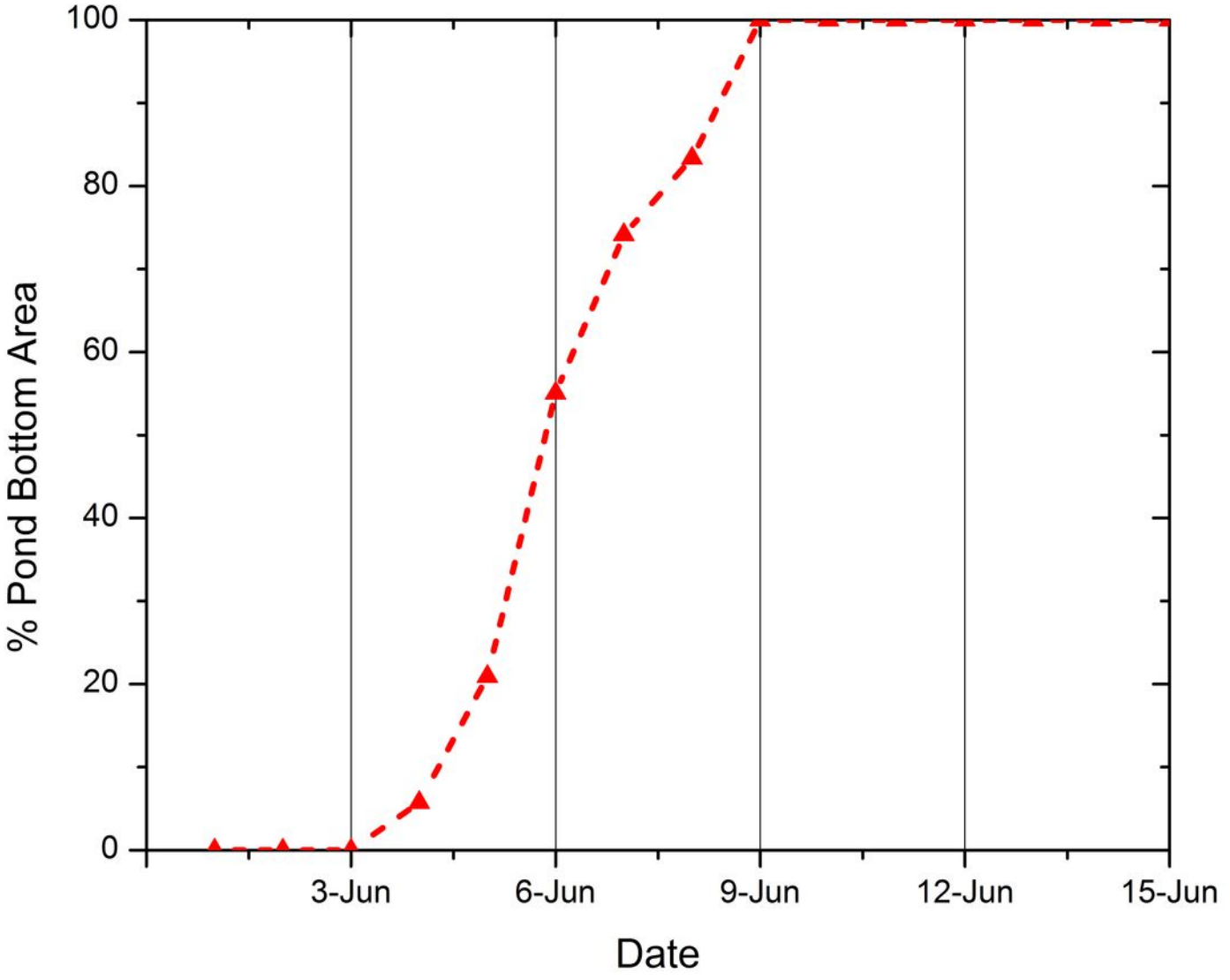
100
80
60
40
20
0
% Pond Bottom Area
3-Jun
6-Jun
9-Jun
12-Jun
15-Jun
Date

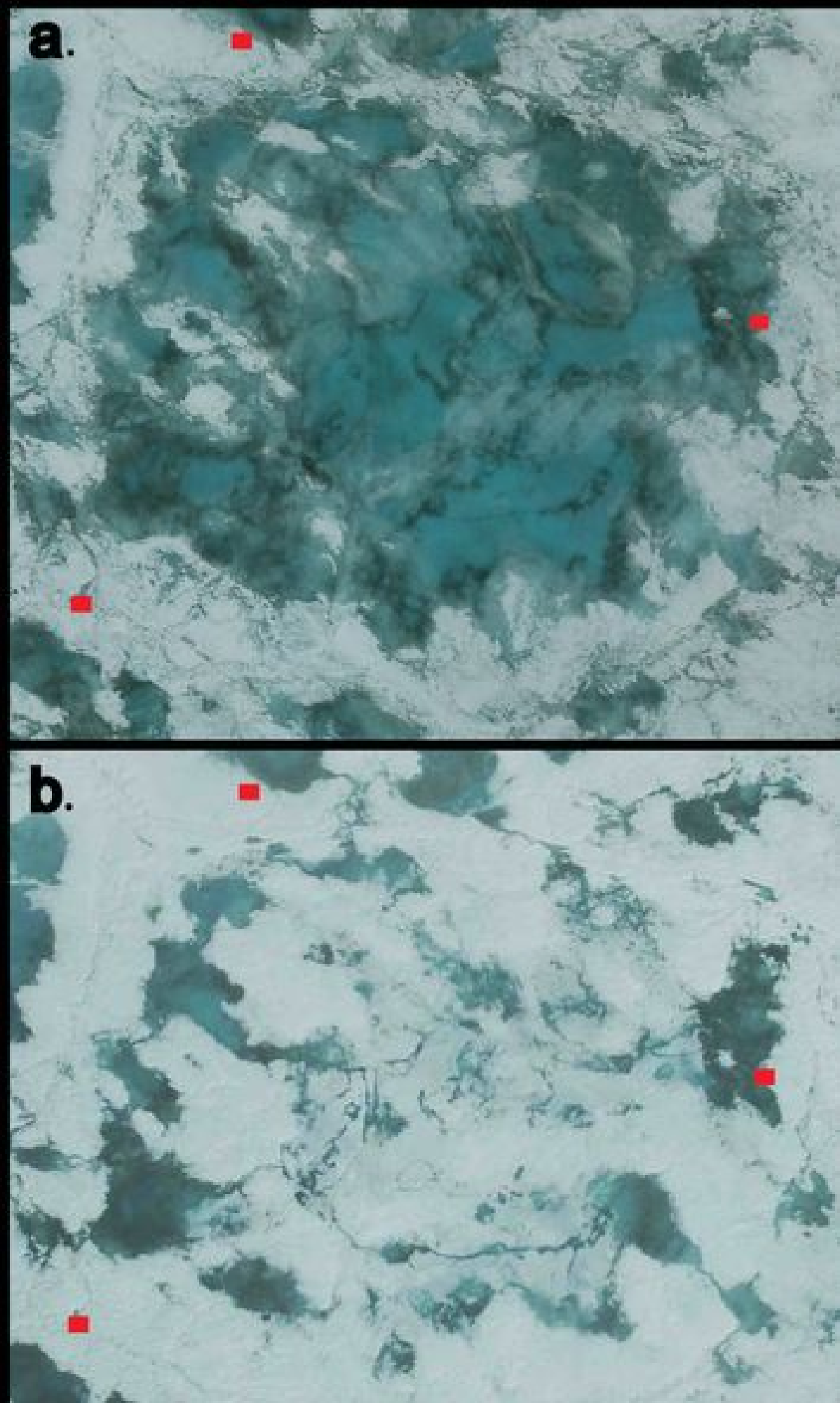
a.
b.

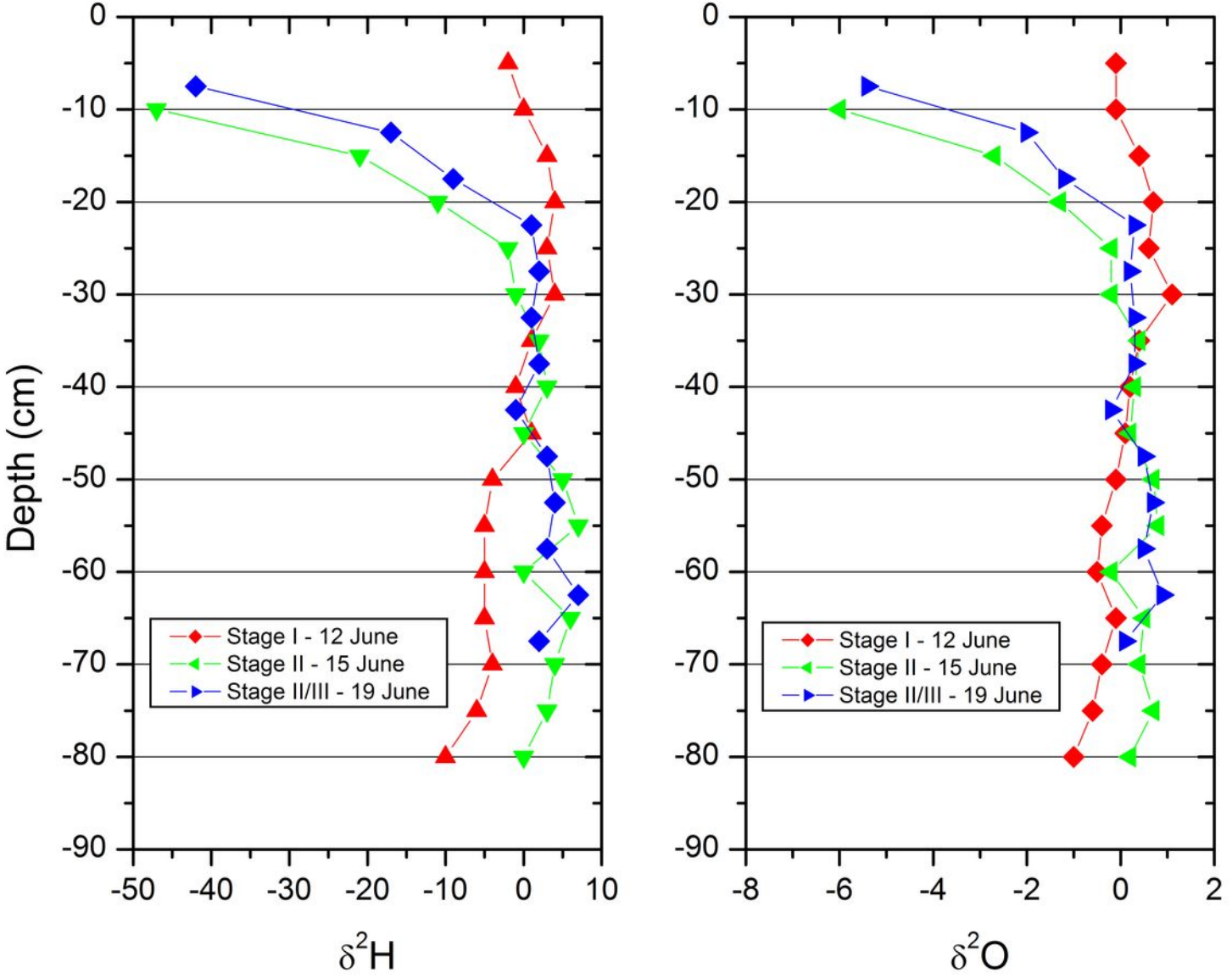
Depth (cm)
0
-10
-20
-30
-40
-50
-60
-70
-80
-90
-50
-40
-30
-20
-10
0
10
δ²H
Stage I - 12 June
Stage II - 15 June
Stage II/III - 19 June
-8
-6
-4
-2
0
2
δ²O

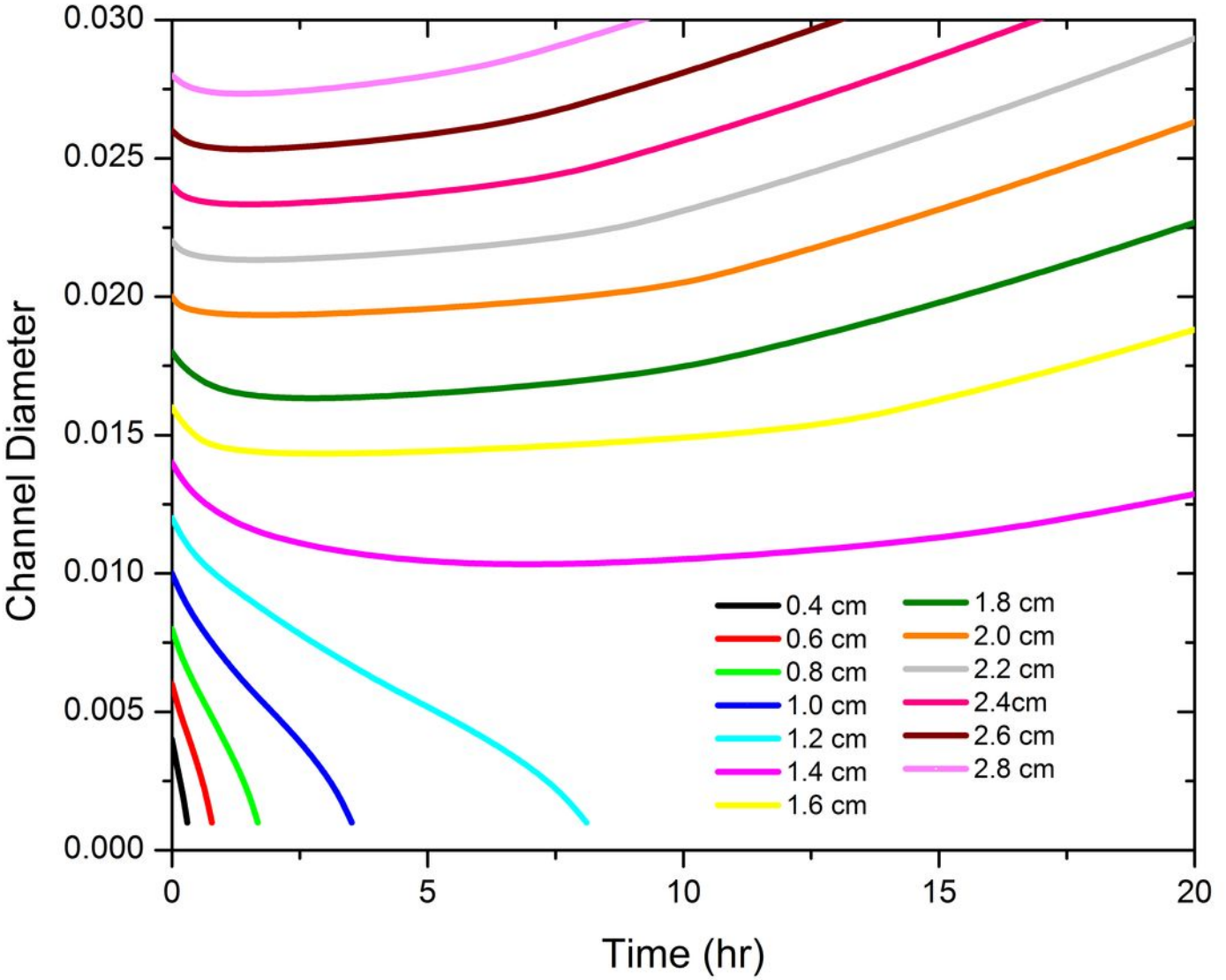
Channel Diameter
0.030
0.025
0.020
0.015
0.010
0.005
0.000
0
5
10
15
20
Time (hr)
0.4 cm
0.6 cm
0.8 cm
1.0 cm
1.2 cm
1.4 cm
1.6 cm
1.8 cm
2.0 cm
2.2 cm
2.4cm
2.6 cm
2.8 cm

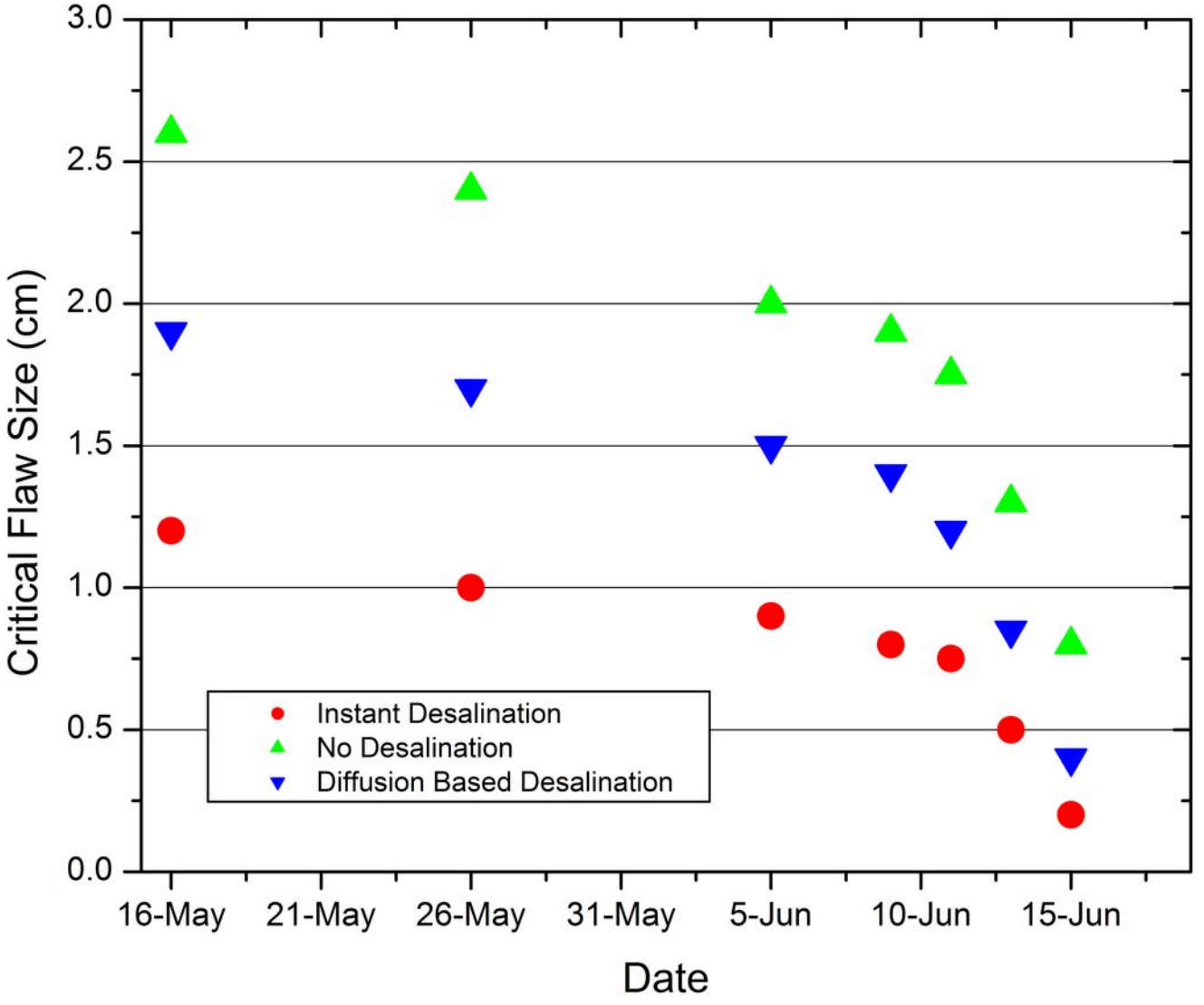
Critical Flaw Size (cm)
3.0
2.5
2.0
1.5
1.0
0.5
0.0
16-May
21-May
26-May
31-May
5-Jun
10-Jun
15-Jun
Date
Instant Desalination
No Desalination
Diffusion Based Desalination